The Synthesis and Characterization of Nano-Sized Rare Earth Oxide Particles and Mesoporous Zirconia

by

Atilla Aşar

A Thesis Submitted to the
Graduate School of Engineering
in Partial Fulfillment of the Requirements for
the Degree of

Master of Science
in
Material Science and Engineering
Koç University

September 2009

Koc University

Graduate School of Sciences and Engineering

This is to certify that I have examined this copy of a master's thesis by

Atilla Aşar

and have found that it is complete and satisfactory in all respects,
and that any and all revisions required by the final
examining committee have been made.

Committee Members:

_____

Mehmet Suat Somer, Ph. D. (Advisor)

_____

Uğur Ünal, Assit. Prof.

_____

Annamaria Miko, Ph. D.

Date: _____

ABSTRACT

The thesis work consists of two main parts. The first one is focused on the synthesis of rare earth oxides having nanometer particle size via two methods: liquid crystal templating and sol-gel method. The samples were characterized by DTA/TG measurements combined with Mass spectroscopy, XRPD, DLS, FTIR and HR-TEM investigations. The average crystalline grain size was calculated from the XRPD data based on the Debye-Scherrer's equation.

The precursors in liquid crystal templating method were rare earth nitrates, $RE(NO_3)_3.nH_2O$ (n = 4-6; RE = Pr, Nd, Sm, Eu, Gd, Dy, Ho, Er, Tm, Yb, Lu) and non-ionic surfactant $C_{12}H_{25}(CH_2CH_2O)_{10}OH$ (Brij 56®) was used as surface-active agent. The XRPD results reveal that all as-prepared samples consist of oxides - hydroxides. The crystalline oxide formation of these rare earths was determined and for most of the investigated elements it took place at ~773 K under constant air flow. Unlike the other investigated elements, neodymium as-prepared sample shows different thermal behavior and forms oxide carbonate, $Nd_2O_2CO_3$, when annealed in the presence of CO_2. The liquid crystal templating resulted oxide nanoparticles with the mean particle size less than 15 nm except Sm_2O_3 where the mean particle size was 23 nm. According to HR-TEM investigations, the oxide nanoparticles possess disordered nanoporous structures.

The second method is based on a modified sol-gel route to prepare nanoparticles of Eu_2O_3, Gd_2O_3 and Er_2O_3. Precipitations of the rare earth hydroxides was achieved for the first time by passing gaseous ammonia trough the suspension of $RE(NO_3)_3.nH_2O$ (n = 4-6; RE = Eu, Gd Er) dispersed in the mixture of diethylene glycol (DEG) and tetraethylene glycol (TEG). The XRPD results showed that, precipitates after gaseous ammonia purge have amorphous structure. The DTA/TG experiments confirmed the oxides formation takes place at ~573 K in one exothermic step in line with the XRPD results. The average particle sizes of the oxides were 10-35 nm. The Eu_2O_3 powders were successfully infiltrated into

Al_2O_3 inverse opals as well. These samples were illuminated by 355 nm laser light and they exhibited red luminescence of Eu_2O_3.

In the second part of the study, nanoporous zirconium oxides were synthesized based on surfactant templating. Two different surface directing agents, cationic hexadecyl-trimethyl-ammonium bromide $CH_3(CH_2)_{15}N(CH_3)_3Br$ (CTAB) and nonionic $C_{12}H_{25}(CH_2CH_2O)_{10}OH$ (Brij56®), were studied. The synthesis was carried out in the presence of two series of precursors, zirconium oxychloride, $ZrOCl_2.8H_2O$ and zirconium (IV) ethoxide, $Zr(OC_2H_5)_4$. The thermal behavior was investigated by DTA/TG and mass spectroscopy measurements. The analysis of the different phases and their chemical composition were studied by XRPD, FTIR and HR-TEM experiments.

In the presence of CTAB, the XRPD and DTA/TG results showed that in both precursor cases the as-prepared amorphous hybrid oxide-hydroxide (containing both inorganic and organic compounds) transforms to crystalline tetragonal zirconium oxide when annealing at 923 K. The FTIR investigations confirmed that organic surfactant decomposes at ~650 K and leaves high purity stable tetragonal phase behind. The HR-TEM results taken from the samples synthesized from $Zr(OC_2H_5)_4$ precursor indicated partial hexagonal pore arrangements after annealed at 723 K. At this temperature, the sample synthesized from $ZrOCl_2.8H_2O$ precursor possessed ordered pore structure and uniform pore size of 2.8 nm with amorphous walls.

In the presence of Brij56 similar to the CTAB system both precursor resulted amorphous oxide-hydroxide. Based on the DTA/TG investigations the organic surfactant decomposed at ~650 K while increasing the temperature to 723 K mainly monoclinic zirconium oxide with some tetragonal phase formed. Further heat treatment at 923 K caused phase transformation to tetragonal form when $ZrOCl_2{\cdot}8H_2O$ was applied as starting material. For the $Zr(OC_2H_5)_4$ precursor some monoclinic phase was also identified in the main tetragonal phase. Similar heat treatment at 723 K results in both cases in formation of porous ZrO2 with a high pore size distribution.

ÖZET

Bu tez çalışması iki ana bölümden oluşmaktadır. Çalışmanın ilk bölümü nadir toprak element (NT) oksitlerinin nano boyutlu parçacıklarının sıvı kristal maskeleme ve sol-jel yöntemleriyle sentezlenmesine odaklanmıştır. Numuneler diferansiyel termal analiz ve termal gravimetri (DTA/TG), kütle spektroskopisi (MS), toz X-ışını kırınımı (XRPD), dinamik ışık saçılımı (DLS), Fourier dönüşüm kızılötesi spektroskopisi (FTIR) ve yüksek çözünürlüklü geçirgen elektron mikroskop (HR-TEM) metotlarıyla karakterize edilmiştir. Ortalama kristal tanecik boyutu Debye-Scherrer denklemi kullanılarak XRPD sonuçlarından hesaplanmıştır.

Sıvı kristal maskeleme metodunda başlangıç maddesi olarak nitratlar, $NT(NO_3)_3.nH_2O$ (n = 4-6; NT = Pr, Nd, Sm, Eu, Gd, Dy, Ho, Er, Tm, Yb, Lu) ve yüzey aktif madde olarak iyonik olmayan $C_{12}H_{25}(CH_2CH_2O)_{10}OH$ (Brij 56®) kullanılmıştır. XRPD sonuçlarına göre ara fazların hepsi oksit ve hidroksitlerden oluşmaktadır. Bu nadir toprak elementlerinin kristal oksitlerinin oluştuğu tespit edilmiş ve araştırılan numunelerin çoğu için bu 773 K'de sabit hava akışı altında gerçekleşmiştir. Diğer numunelerden farklı olarak, neodyum ara fazı farklı termal özelliklere sahiptir ve CO_2 varlığında tavlandığında oksit karbonat, $Nd_2O_2CO_3$ oluşturmuştur. Sıvı kristal maskeleme sonucu ortalama parçacık boyutu 15 nm'den küçük olan oksit nanoparçacıklar elde edilmiştir ancak Sm_2O_3 için bu değer 23 nm'dir. HR-TEM bulgularına göre, oksit nanoparçacıklar düzensiz nano-gözenekli yapıya sahiptirler.

İkinci yöntem, Eu_2O_3, Gd_2O_3 ve Er_2O_3 nanoparçacıklarının geliştirilmiş sol-jel metoduyla hazırlanmasına dayanmaktadır. Nadir toprak element hidroksitlerinin çökeltisi gaz amonyağın dietilen glikol ve tetraetilen glikol karışımı içerisinde dağılmış olan $NT(NO_3)_3.nH_2O$ (n = 4-6; NT = Eu, Gd, Er) süspansiyonundan geçirilerek ilk kez başarılmıştır. XRPD sonuçları gaz geçirildikten sonra oluşan çökeltilerin amorf bir yapıya sahip olduğunu göstermiştir. DTA/TG deneyleri, XRPD sonuçlarıyla beraber ~573 K'de

tek ekzotermik adımda gerçekleşen oksit oluşumunu doğrulamıştır. Bu oksitlerin ortalama parçacık boyutu 10-35 nm'dir. Ayrıca sentezlenen Eu_2O_3 tozu başarıyla Al_2O_3 ters opalların içine nüfuz ettirilmiştir. Bu numuneler 355 nm'lik lazer ışığı ile aydınlatılmıştır ve Eu_2O_3'ın kırmızı ışıldamasını sergilemiştir.

Çalışmanın ikinci bölümünde ise, nano-gözenekli zirkonyum oksitler surfaktan maskeleme metoduna dayanarak sentezlenmiştir. Katyonik heksadesiltrimetilamonyum bromür, $CH_3(CH_2)_{15}N(CH_3)_3Br$ (CTAB) ve iyonik olmayan, $C_{12}H_{25}(CH_2CH_2O)_{10}OH$ (Brij56®) olmak üzere iki farklı yüzey-yönlendirici maddeyle çalışılmıştır. Sentez iki dizi başlangıç maddesi, zirkonyum okso klorür, $ZrOCl_2.8H_2O$ ve zirkonyum (IV) etoksit, $Zr(OC_2H_5)_4$ varlığında gerçekleştirilmiştir. Numunelerin termal özellikleri DTA/TG ve MS metotlarıyla incelenmiştir. Farklı fazların ve bunların kimyasal bileşimlerinin analizi XRPD, FTIR ve HR-TEM ölçümleriyle yapılmıştır.

CTAB varlığında, XRPD ve DTA/TG sonuçları göstermiştir ki farklı başlangıç maddesiyle hazırlanan her iki melez oksit-hidroksit ara fazı (organik ve anorganik bileşiklerin her ikisini de içeren) 923 K'de tavlandığında tetragonal zirkonyum okside dönüşmüştür. FTIR araştırmaları organik surfaktanın 650 K'de bozulduğunu ve geride yüksek saflıkta kararlı tetragonal faz bıraktığını doğrulamıştır. $Zr(OC_2H_5)_4$ başlangıç maddesiyle sentezlenen numunelerin 723 K'de tavlandıktan sonra alınan HR-TEM sonuçları kısmi hegzagonal gözenek yapıyı göstermiştir. Bu sıcaklıkta, $ZrOCl_2.8H_2O$ başlangıç maddesiyle sentezlenen numune 2,8 nm boyutlarında düzenli ve tek biçimli gözenek yapısıyla beraber amorf gözenek duvarlara sahiptir.

Brij56® varlığında, CTAB sistemine benzer bir şekilde her iki başlangıç maddesi de melez oksit-hidroksit ara fazı meydana getirmiştir. DTA/TG araştırmalarına göre organik surfaktan ~650 K'de bozulmakla beraber sıcaklığın 723 K'e yükseltilmesiyle başta monoklinik ve tetragonal zirkonyum oksit fazları oluşmuştur. 923 K'de yapılan ilave ısı uygulaması, $ZrOCl_2 \cdot 8H_2O$ başlangıç maddesi olarak kullanıldığında tetragonal faz değişimine neden olmuştur. $Zr(OC_2H_5)_4$ başlangıç maddesinde ise ana tetragonal fazda aynı

zamanda monoklinik faz bulunmuştur. 723 K'deki benzer ısı uygulamaları her iki koşulda da yüksek boyut dağılımlı gözenekli yapıların oluşmasıyla sonuçlanmıştır.

ACKNOWLEDGEMENTS

I would like to express my sincere appreciate to my supervisor, Prof. Dr. Mehmet Somer, who has supported me throughout my undergraduate and M.Sc. studies. I always felt encouraged by his moral support during sevens years in Koç University.

My special thanks go to Dr. Annamaria Miko for not only being my committee member, but also for her help in writing my M.Sc. thesis work.

Also, I would like to express my gratitude to Prof. Dr. Cefe Lopez and Dr. Alvaro Blanco for letting me to work in their laboratory in Institute of Material Science Madrid. It was pleasure to work with them in a very friendly and amusing environment. I am grateful to PhOREMOST for its generous financial support during my stay in fantastic Madrid.

I am indebted to my colleagues and also my friends, Sinan Öztürk, İlkin Kokal, Kamil Kiraz, Semih Afyon, Selin Seheryıldızı, Kerem Kaya, Ali Baş and Burcu Uslu, for supporting me in numerous ways. Especially, I would like to thank my flat mate Selçuk Acar and my office-mate Cevriye Koz for making the laboratory life bearable.

I want to express my gratitude to Muharrem Usta for his amazing talent in glass works and his fatherly attitude.

Finally and most importantly, I would like to thank my parents Sema and Erdoğan Aşar and my lovely brother Alper Aşar for their endless love and their unconditional support.

I am very grateful to “mia Angela“ Yasemin for making my life meaningful. Without her persistent confidence and understanding I would never have completed my work.

TABLE OF CONTENTS

LIST OF FIGURES

LIST OF TABLES

NOMENCLATURE

ALD: Atomic Layer Deposition

ΔT: Temperature difference

a.u.: Arbitrary Unit

DSC: Differential Scanning Calorimetry

DTA: Differential Thermal Analysis

DLS: Dynamic Light Scattering

FFT: Fast Fourier Transform

FTIR: Fourier Transform Infra Red

HR-TEM: High Resolution Transmission Electron Microscopy

NCT: Neutron Capture Therapy

m/e: Mass to charge ratio

MCM: Mobile Crystalline Material

MID: Multiple Ion Detection

MS: Mass Spectroscopy

PCs: Photonic Crystals

RT: Room Temperature

SOFC: Solid Oxide Fuel Cell

TG: Thermal Gravimetry

XRD: X-Ray Diffraction

XRPD: X-Ray Powder Diffraction

Chapter 1

INTRODUCTION

1.1. Introduction to Nanoscale Materials

Nanoscale materials or nanomaterials can be defined as materials whose characteristic length scale or structure size is hundred nanometer or smaller. This definition is very broad and includes any substances such as metals, semiconductors and organic polymers in any kind of structure like core-shell composite architectures, or nanotubes or mesoporous materials.

Nanomaterials are fascinating because within this scale, atoms and molecules interact and assembled into structures that the chemical and physical properties of matter are significantly unique compared to their individual atoms or molecules of their corresponding bulk counterparts. These unique properties are depend on changes in physical attributes (size, shape and specific surface area) [1, 2]. Indeed, two of the major factors why nanomaterials show properties different from those of bulk are size-dependent effects: the increase in the ratio of atoms at the surface and quantum effects which show discontinuous behavior due to completion of shells in the systems with delocalized electrons [3].

As a general rule, the smaller a particle becomes, the ratio of surface area to volume increases, and therefore the larger the fraction of their constituents atoms are located at the surface. For example, a 3 nm iron particle has approximately 50% of its atoms on the surface, whereas a 10 nm particle has just 20% on the surface, and a 30 nm particle only 5% [4]. Because of these, the behavior of atoms on the surface becomes dominant over that of those in the interior of the particle. Surface atoms are less stabilized than interior atoms,

because surface atoms have fewer neighbors which lead to lower coordination and unsatisfied bonds [5]. This affects both the properties of the particle in isolation and its interaction with other materials. The lower melting point of surface layers is a consequence of lower stabilization of atoms or molecules at the surfaces.

In addition, once particles have dimensions in the nanoscale, they start to exhibit quantum mechanical behavior. In metals and semiconductors densities of state and the energies of the particles depend crucially on the size of the particle. However, discontinuities come when the states are filled up, and a new shell at higher energy starts to be populated (Fig. 1.1) [5]. As result of these discontinuities there is no simple scaling; instead there is a behavior similar to atoms, with filled shells of extra stability. Therefore, emission lifetime [6], fluorescence wavelengths [7], and concentration quenching [8] become strongly depend on the particle-size in the nanometer range [5]. In Fig. 1.2, tuning of the fluorescence of CdSe nanocrystals with controlling their diameters is illustrated [9].

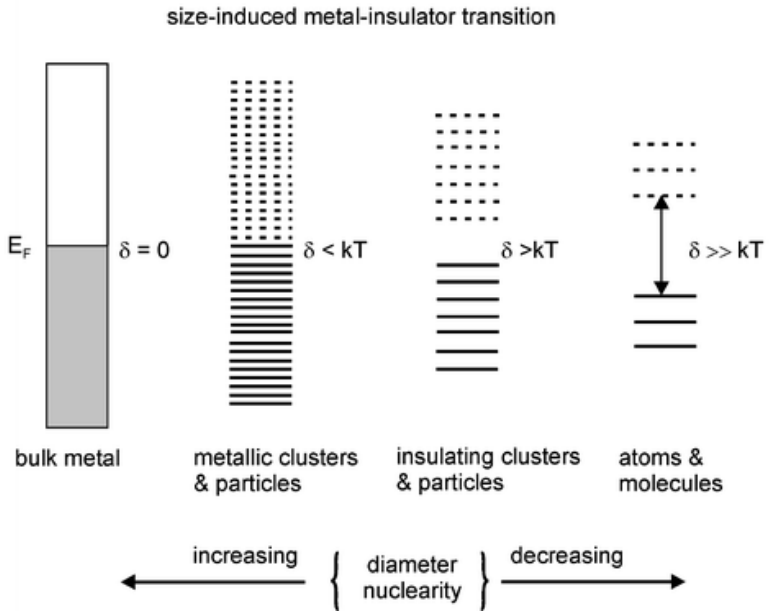

Fig. 1.1 The development of the density of state and evolution of the band gap with increasing number of atoms in a system [5]

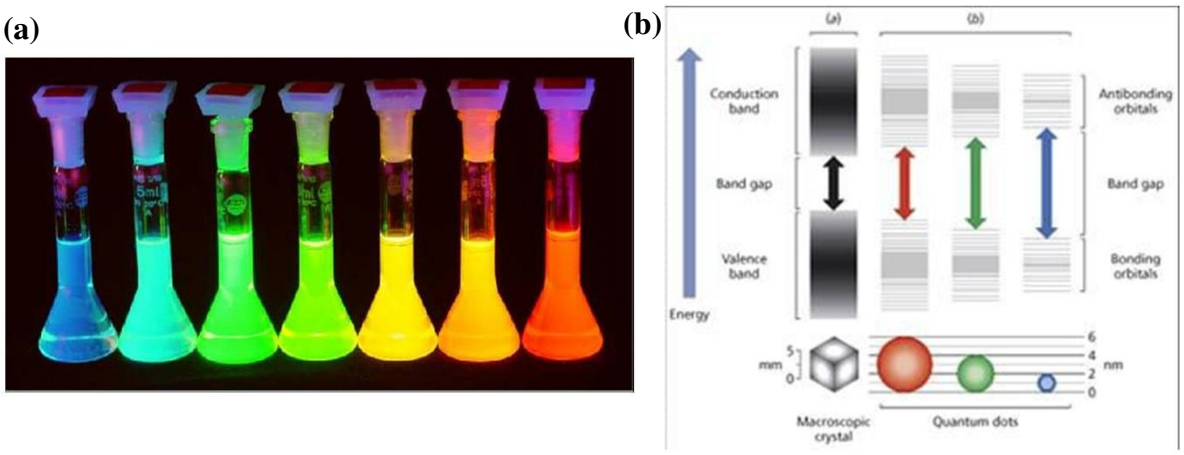

Fig. 1.2 (a) Fluorescence of monodisperse CdSe nanocrystals with increasing diameter (2 to 7 nm) from left to right, evidence of the scalling of the semiconductor band gap with particle size. (b) Schematic representation of the size effect on the semiconductor band gap [9]

As a result of controlling particle dimensions in nanometer range and assembly of the constituents, one can alter or prescribe thermodynamic, mechanical, optical, chemical and magnetic properties of nanomaterials relative to their bulk counterparts. As more than one of these properties may change in the same particle, nanomaterials with a range of functionalities can be designed and tailor-made at the molecular level to have desired functionalities and properties for targeted applications.

An abundance of scientific data is available to make useful comparisons between nanoscale materials and their bulk materials. For example, the water solubility of Gadolinium acetylacetonate (GdAcAc), a potential anticancer agent for neutron capture therapy (NCT), increased more than 2000-fold by entrapping in stable nanoparticles [10]. Silicone nanospheres (20-50 nm) have hardness four times greater than those of bulk

silicone (50 Gpa *cf.* 12 Gpa) [11]. The luminescence efficiency of Europium oxide nanocrystals increases by a factor of five when the particle size is reduced from 40 to 2 nm [12]. Although, Palladium and Platinum elements are not magnetic in the bulk, nanoparticles comprising several hundred atoms of Pd and Pt embedded in a polymer revealed magnetic moments [13].

1.1.1. Rare Earth Oxides

Rare earth elements, the third subgroup in the periodic table, includes 15 elements from 57^{th} to 71^{st} atomic number of lanthanide elements (Ln), such as lanthanum (La), cerium (Ce), praseodymium (Pr), neodymium (Nd), promethium (^{147}Pm), samarium (Sm), europium (Eu), gadolinium (Gd), terbium (Tb), dysprosium (Dy), holmium (Ho), erbium (Er), thulium (Tm), ytterbium (Yb), Lutetium (Lu), in ascending order of atomic numbers, and scandium (Sc) and yttrium (Y) elements, a total of 17 elements. According to physical and chemical properties, these elements can be divided into the "cerium group" or "light earths" (La to Eu) and the "yttrium group" or "heavy earths" (Gd to Lu, plus Y) [14].

With the exceptions of the unstable promethium, rare earth elements can be found in relatively high-concentration in the Earth's crust. These elements range in crustal abundance from Ce, the 25^{th} most abundant of all elements with 66 ppm to Tm [14].

Due to the f-f orbital transitions of electrons, rare earth elements have varied electronic energy levels and spectra. They can absorb or emit light of various wavelengths. Indeed, they have high photostability, long luminescent lifetime (~1 ms), narrow emission bands and large Stokes shift [15].

In accordance with their relatively low atomization enthalpies and ionization potentials, the lanthanide elements are very reactive. Many of lanthanide elements show oxidation state of +3, a common characteristic chemical feature of these elements and the

corresponding sesquioxides like Ln_2O_3 exist for all of them [14]. Seldom Ce, Pr, and Tb elements occur in +4 oxidation state as well [16].

1.1.2. Synthesis and Preparation Methods of Rare Earth Oxides Nanoparticles

With the development in nanotechnology, nano-sized rare earth oxides become essential in various industrial applications such as high performance luminescent devices, energy storage devices, magnets and catalysts because of their electronic, optical and chemical characteristics. The smaller the particles size of the individual nanoparticles, the larger the specific surface area which can result in higher chemical activity. Therefore, the properties of rare earth oxides can be tailored with synthesizing them in nanometer scales at different crystalline grain size.

Various techniques for the synthesis and preparation of nano-sized rare earth oxides have been developed. In this section, selected method for the synthesis of fine particles built up from rare earth oxides is presented.

Gas Phase Condensation

During this method, precursor (mostly a metal) is vaporized by high-power lasers or sputtering in various gas atmospheres. The vapor of precursor collides with the gas atoms of the atmosphere and nanoparticles are formed by the subsequent condensation on a cold surface. For example, in an oxygen atmosphere, the precursor reacts with oxygen forming metal oxide nanoparticles, while in an inert atmosphere, metal nanoparticles are formed. The characteristic of the particles depend on total pressure, gas flow rate, evaporation rate and gas composition [17]. This method has been applied to the preparation of rare earth oxides doped phosphor particles [18, 19].

Precipitation Method

This method has ranged from simple precipitation (heterogeneous) reactions to much more complex self assembly based (homogeneous) precipitation routes. The general

mechanism involves precipitation of nanoparticles after the solution reached the critical supersaturation threshold. In general simple precipitation results in high size distribution and agglomerated nanoparticles. To improve this disadvantage, a self assembly based route has been developed in which the production of the precipitant is controlled from another chemical source in the solution. Liquid crystal templating and sol-gel techniques are based on precipitation method. Self-assembled templating agents are used to control the structure of nanostructured materials in liquid crystal templating. The self-assembled structure of liquid crystal leads to growing of inorganic material in a control manner. In sol-gel technique, non-aqueous solvents such as polyalcohols can be used as a stabilizer. These solvents have high viscosity and these decay the transport of the inorganic substances and prevent the growth of inorganic particles [20, 21].

Hydrothermal and Solvothermal Methods

In this method, under high temperatures (>80 °C) and high pressures (>1 atm), precursor material transformation takes place in water medium in a sealed system. The boiling point of water is elevated by the pressure that is generated due to the water vapor. The phase transformation, particle size and shape can be controlled by tuning the parameters such as water pressure, temperature, reaction time and respective precursor-product system.

Not only water, but also ammonia water or some organic solvents can be used as reaction media, which is generally called a solvothermal method. Many researchers reported on the rare earth oxides prepared with hydrothermal and solvothermal methods [22-24].

Spray Pyrolysis

This method is a traditional deposition method based on solution process and has been widely used in industry. This process simply consists of converting microsized liquid droplets of precursor into solid particles through heating under controlled atmosphere at

elevated temperatures. When the droplets are heated in air, first evaporation of the solvent takes place and simultaneously precursor is converted to its oxides. By this method, the rare earth oxides are quenched at an early stage of crystal growth [25-27].

1.1.3. Rare Earth Oxide Applications

Due to their electronic, optical and chemical properties, nanostructured rare earth oxides become more important for industrial and technological applications. There are numerous applications of rare earth oxide nanoparticles either on the market or under development. Table 1 summarizes some current applications and some recently published scientific achievements which rely on rare earth oxides [16, 28].

Table 1 Selected current and future applications of nanoparticles [16, 28]

Industry	Materials/Opportunity	Advantages of Nanomaterials
Power/Energy	The latest solid oxide fuel cells (SOFC) uses nanostructured rare earth oxide doped ZrO_2 for solid electrolyte, electrodes and interconnectors.	SOFC with Sc stabilized zirconia are very advantageous in operating temperature, and energy storage than conventional plates [29].

Machine tools	Rare earth oxides coated tool bits for cutting and drilling.	Nanocrystalline metal oxide (Nd_2O_3, CeO_2,) materials provide harder and longer lasting materials.
	Rare earth oxides for improved ceramics.	Conventional ceramics can be made abrasion-resistant and easier to work through the addition of nano-sized rare earth oxides [30].
Automotive	Nanocrystalline rare earth oxides have been used in automotive components for altering their properties.	Better chemical and mechanical properties for automotive components. Fuel additives/nanocatalysts for fuel efficiency.
	Nanocrystalline rare earth oxides doped ceramic liners for engine cylinders.	Nanocrystalline liners that improve efficiency of combustion with retraining heat in cylinders.

Healthcare/ Medicine	Nanostructured rare earth oxides are used for biological labeling.	Rare earth nanocrystals, $Y_2O_3:Eu^{3+}$, low toxicity, hygienic, easy analyzing at low concentration [27].
Electronics	Nanoparticles of rare earth oxide used to improve data-storage	Nanoscale magnetic nanoparticles provide high-density, fast data storage.
	Nano-engineered rare earth oxides for field emission displays.	Rare earth oxides are excellent field emitters.
		Rare earth based tri-phosphor fluorescent lamps Cathode ray tubes (CRT)
Environmental	Improved desulfurizer and denitrifier by doping rare earth oxides.	Mixture of CeO_2 and La_2O_3 catalysts to accelerate the deoxidization of SO_2 and CO [31].
	Rare earth oxides for automobile exhaust-gas convertors	Rare earth perovskite $LaBO_3$ for decomposition of N_2O.

1.2. Introduction to Nanoporous Materials

Porous materials are material containing pores and can be classified depending on their pore diameter. According to the International Union of Pure and Applied Chemistry (IUPAC) conventions, porous materials are classified based on their pore diameters as follows [32]:

- Microporous Materials

Pore diameters are in the range of 2 nm and below

- Mesoporous Materials

Pore diameters are between 2 nm to 50 nm

- Macroporous Materials

Pore diameters are larger than about 50 nm

In general, the fraction of pore volume to the total volume in porous materials is in the range of 0.2-0.95 [33]. Due to their enlarged surface area induced by the porosity in the material advantageous properties such as narrow pore size distribution, large pore volume and high specific surface area can be achieved.

In Fig. 1.3, three different pore systems of porous silica are shown [34]. Although the pore systems of the silica are ordered in these cases, microporous, mesoporous and macroporous materials can have random, disordered pore distribution.

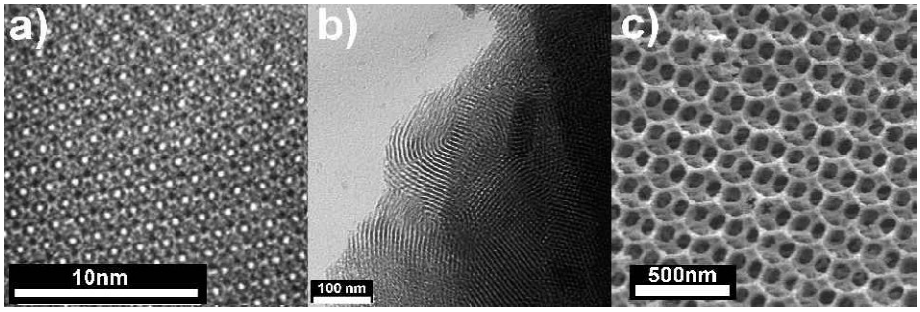

Fig. 1. Error! No text of specified style in document.**3** Different types of porous silica materials (a) microporous, (b) mesoporous, (c) macroporous [34]

Since the groundbreaking papers by Kresge and co-workers introducing the M41S (mesoporous molecular sieves) family of ordered mesoporous silica at the early 1990s [35], the research field dealing with the controlled design of porous materials with nanometer scale has attracted considerable attention and expanded enormously. These materials have specifically a high surface to volume ratio, with a high surface area and large porosity, and very ordered, uniform pore structure. These properties offer great potential for applications in separations, photonics, optics, sensing and catalysis [36].

In addition to the silica mesoporous materials, many researchers have been focused on extending the synthesis strategies from silica mesophases to other materials, particularly ordered porous transition metal oxides. Unlike silica, most of the transition metal compounds exhibit various oxidation states which can be associated with unique magnetic, electronic and optical properties.

Because of its high refractive index, optical transparency, mechanical strength, wear resistance chemical and thermal stability, zirconium oxide (ZrO_2), also called zirconia, has potential uses in wide applications areas [14, 37]. Zirconia is an amphoteric material providing high activity in reactions requiring acid-base bifunctional catalysts [38]. Furthermore, zirconia has a very small phonon energy, which enables its uses as support for luminescent ions, like rare earth ions, making this material suitable for photonic applications [39].

Material properties of zirconia can be tailored by rare-earth dopants to suit different demands for technological applications. For example, porous zirconia used as a catalytic support in automotive exhaust three way catalysts. Doping these materials with rare earth elements improves the structural stability and therefore sintering the material at high temperatures is not necessary. Furthermore, since rare earths, except for Ce^{4+}, have 3 valances which is a lower valence than the Zr^{4+} ions, oxygen vacancies are formed in the lattice to preserve the overall electronic neutrality. As a result, these vacancies give rise to

adsorption sites, ionic conductivity and strong metal-support interactions that are needed for effective catalytic functions [16].

1.3. Scope of the Thesis

This study composed of mainly two parts.

1) In the first part, nano-sized rare earth oxides were prepared via two different methods: liquid crystal templating and sol-gel.

Liquid crystal templating is a synthesis route for preparation nanostructured materials in which the self-assembled structure of a liquid crystal is exploited to control the structure of a growing inorganic material [40]. The liquid crystal templating with the non-ionic surfactant (C_nEO_m) was first used in a "one-pot" synthesis to incorporate Li^+ and Ag^+ ions into mesoporous silica materials by Dag et al. [41, 42]. The surfactant (C_nEO_m) have been generally used for the production of mesoporous and mesostructured materials because the main structures of metal salt mesophases prepared with this surfactant are stable. They maintained their structure unless surfactant is removed from the system [43, 44]. Recently, Dag et al. demonstrated that this technique can be applied successfully on the production of nanoporous transition metal sulfides and TiO_2 [45, 46]. In this system, several transition metal aqua complex salts were dissolved in non-ionic surfactant (C_nEO_m) and the coordinated water molecules of the metal precursors mediate the formation of a hexagonal or cubic liquid crystal mesophases depending on their counter ions [47]. On the other hand, this synthesis route is only suitable for the preparation of metal oxides, whose compounds can be easily hydrolyzed. For this reason, a new synthesis path was developed based on liquid crystal templating for the preparation of rare earth oxides having less preferably hydrolysable compounds.

Nano-sized rare earth oxide particles were prepared by passing gaseous ammonia through the liquid crystalline mesophases to form rare earth hydroxides and heat treatment

results in the formation of their oxides. Hereby, the first successful application of liquid crystal template method with the non-ionic surfactant $C_{12}H_{25}(CH_2CH_2O)_{10}OH$, dodecyl(ethylene oxide) for the production of nano-sized rare earth oxides is presented.

The sol-gel synthesis of rare earth oxides has been reported by Mazdiyasni and Brown for the first time in 1971 [48]. The sol-gel method is based on hydrolysis and condensation reactions and generally, both reactions are fast and proceed at once. Indeed, for the preparation of metal oxides through sol-gel synthesis, two-step conventional heating process is applied. As Feldman et al. stated, the mixture must be heated at 353 K after the dissolution of salt and eventually at 453 K for 2 h [49]. This conventional heating method is time and energy consuming. Therefore, to synthesize nano-sized rare earth oxides at a lower temperature with a reduced preparation time, the sol-gel method has to be improved. Nanoparticles of Eu_2O_3, Gd_2O_3 and Er_2O_3 were synthesized by this improved method. The rare earth nitrate salts were dissolved in diethylene glycol (DEG) and tetraethylene glycol (TEG) polyalcohol mixture, in which high viscosity and steric hindrance inhibits the agglomeration of the particles. After hydrolysis, with passing gaseous ammonia through the mixture, formation of rare earth hydroxides intermediate phases took place and they were decomposed to their oxides by annealing.

2) In the second part, two synthesis system based on surfactant templating method were employed to prepare mesoporous zirconia.

After Hudson and Knowles reported the first preparation of zirconium based mesoporous materials [50], many methods have been explored to mesoporous zirconia powders such as sol-gel method [51], solid state reaction method [52] and CO_2 supercritical drying [53]. Among these methods, surfactant templating allow construction of materials with control structural characteristics on a nanometer scale. Ciesla et al. demonstrated ordered hexagonal mesoporous zirconium oxide-sulfate and zirconium oxo phosphate prepared by surfactant templating method. This sample possessed a pore quality equal to

that of MCM-41 (Mobile Crystalline Material) [54]. The first ordered mesoporous zirconia prepared by surfactant templating method was published by Crepaldi et al. [55].

In the first method, hydrothermal synthesis method assisted with surfactant templating was used. In this system, the ordered mesoporous zirconia with cationic surfactant hexadecyl-trimethyl-ammonium bromide, CTAB was produced. For the preparation of mesoporous zirconia, the method which was published by Ciesla et al. was improved [54]. Electrostatic interaction between cationic head group of CTAB and zirconium precursor mediates zirconium salts to form continuous mesophases around micellar rods of CTAB. Removal of the surfactant through annealing resulted in the formation of ordered mesoporous zirconia. In the second method, liquid crystal templating with non-ionic surfactant (C_nEO_m) was applied. Besides the synthesis based on ionic interactions, the liquid crystal approach was investigated. The synthesis path for the preparation of mesoporous zirconia with uniform and ordered pore structures was similar to the liquid crystal templating method performed for the synthesis of nano-sized rare earth oxides. In this approach hydrogen bonding is the driving force of the mesophases.

Chapter 2

SYNTHESIS & CHARACTERIZATION

2.1. Synthesis of Nano-Sized Rare Earth Oxides

2.1.1. Liquid Crystal Templating Method

The precursors in liquid crystal templating method were hydrous rare earth nitrate salts, $RE(NO_3)_3.nH_2O$ (n = 4-6; RE = Pr, Nd, Sm, Eu, Gd, Dy, Ho, Er, Tm, Yb, Lu) and oligo(ethylene oxide) type non-ionic surfactant, $C_{12}H_{25}(CH_2CH_2O)_{10}OH$, dodecyl(ethylene oxide), denoted as Brij56® was used as a surface-active agent.

For the preparation of the samples, $RE(NO_3)_3$ was dissolved in melted Brij56®. Several molar ratios of salt to surfactant were tested with varying surfactants having different tail sizes. In the salt rich mixtures (2:1, 4:1 and 6:1), rare earth salt first dissolved in a 1:1 mixture of ethanol and water prior to mixing with the melted surfactant. In the surfactant rich ones (1:6, 1:4 and 1:2), the salt was dissolved in the melted surfactant in a solvent free medium.

For the optimization of the salt-surfactant ratio, samples obtained from mixtures with different ratios were analyzed with XRPD. Based on the results, 1:6 molar ratio was the most effective for the synthesis of well dispersed fine nanoparticles. Therefore, this ratio was used for the preparation of well dispersed fine nanoparticles.

Rare earth nitrate salt and surfactant were mixed in a sonicator at 333 K. This results in the formation of liquid crystalline mesophases of surfactant and salt. Afterward, gaseous

ammonia was passed through the liquid crystalline mesophase, yielding a gelatinous precipitate. To have a uniform distribution, gaseous ammonia was chosen as OH^- source. The precipitate was washed with an ethanol/diethyl ether mixture for the removal of the surfactant and unwanted ions. Further, the precipitate was dried in oven at 343 K.

In the last step the crude powders were annealed at 773 K for 24 h so as to remove any surfactant residual and decompose as-prepared (dried) rare earth hydroxide samples and obtain nano-sized rare earth oxide.

Overall reactions taking place during the synthesis of nano-sized rare earth oxides can be summarized as follows:

$$-\ NH_{3(g)} + H_2O\ (\text{coordinated}) \rightarrow NH_4^+ + OH^-$$

$$-\ [RE(H_2O)_6]^{3+} + OH^- \rightarrow [RE(H_2O)_5(OH)]^{2+} + H_2O$$

$$-\ [RE(H_2O)_5(OH)]^{2+} + OH^- \rightarrow [RE(H_2O)_4(OH)_2]^+ + H_2O$$

$$-\ [RE(H_2O)_4(OH)_2]^+ + OH^- \rightarrow RE(OH)_3 + 4H_2O$$

$$-\ (OH)_2RE{-}OH + OH{-}RE(OH)_2 \rightarrow (OH)_2RE{-}O{-}RE(OH)_2 + H_2O$$

2.1.2. Sol-Gel Method

Several polyalcohols such as ethylene glycol (EG), diethylene glycol (DEG), tetraethylene glycol (TEG), polyethylene glycol (PEG) and their mixtures with varying salt-solvent ratios were tested by our group for the optimization of the proper solvent and salt to solvent ratio. Based on DLS analysis, well dispersed nanoparticles were obtained by the mixture of DEG and TEG with1:1 volume ratio.

A mixture of diethylene glycol (DEG) and tetraethylene glycol (TEG) at a 1:1 volume ratio was prepared. This mixture was added onto precursor, hydrous rare earth nitrate salt, $RE(NO_3)_3.nH_2O$ (n = 4-6; RE = Eu, Gd Er) to form a polyol solution of 0.04 mol/L, which

was stirred vigorously in a round bottom flask at room temperature. After dissolving rare earth nitrate salt, the mixture was heated under constant stirring at 353 K for 1 h in an oil bath. In order to prevent evaporation of the solution, a condenser was placed onto the synthesis flask. At this temperature, an appropriate amount of water is added into the mixture to hydrolyze the salt and form a dispersion of colloidal particles. Subsequently, gaseous ammonia was passed through the resulting homogeneous mixture while stirring at room temperature, which induced the formation of gelatinous precipitation of rare earth hydroxide. The precipitate was washed with an isopropyl alcohol (IPA) for the removal of the (DEG)-(TEG) mixture and unwanted ions. Further, the precipitate was dried in oven at 343 K.

In the last step the crude powders were annealed at 773 K for 24 h to remove any surfactant residual and decompose as-prepared (dried) rare earth hydroxide samples and obtain nano-sized rare earth oxide.

2.2. Synthesis of Porous Zirconia

Porous zirconium oxides were prepared through surfactant templating route by using two series of surfactant. In the first method, cationic surfactant hexadecyl-trimethyl-ammonium bromide, $CH_3(CH_2)_{15}N(CH_3)_3Br$ (CTAB) and in the second method, non-ionic surfactant dodecyl(ethylene oxide), Brij56® was used as a templating agent. In both surfactant case two different precursors; zirconium oxychloride, $ZrOCl_2.8H_2O$ and zirconium (IV) ethoxide, $Zr(OC_2H_5)_4$ was investigated.

In the first method, 0.02 mol of CTAB was dissolved in 50 ml hot water and 40 ml 1 M H_2SO_4 was added into it. This solution was mixed with aqueous solution containing 0.04 mol $ZrOCl_2.8H_2O$. The mixture was stirred at room temperature for 6 h. The solution was further transferred into a Teflon autoclave and hydrothermally treated at 373 K for 24 h. At room temperature, the pH value of the solution was adjusted to 2-3 by adding

1 M NaOH solution. The reactants were then heated at 373 K for 48 h in order to form network between zirconium sites. The as-prepared product was washed with ethanol and water mixture to remove the surfactant and dried in oven at 343 K for 12 h. The crude powders were annealed at 723 K for 5 h. The same procedure was repeated for $Zr(OC_2H_5)_4$ precursor.

In the second method, for the preparation of the samples, the precursor was dissolved in melted Brij56® with the optimized precursor-surfactant molar ratio 1:6. The zirconium precursor and surfactant were mixed in a sonicator at 333 K and gaseous ammonia was passed through the liquid crystalline mesophase, yielding a gelatinous precipitate. The precipitate was washed with an ethanol/diethyl ether mixture and dried in oven at 343 K. In the last step the crude powders were annealed at 773 K for 24 h.

2.3. Characterization Techniques

2.3.1. X-ray Powder Diffraction

For the phase analysis of the samples, XRPD was used. Spatula tip of fine ground powder of samples was sandwiched between to Mylar® Polyester films by using aluminum sample holder.

The XRPD patterns for the samples were recorded by an Imaging Plate Guinier Diffractometer 670 using Cu$K\alpha_1$ (λ = 1.5405 Å) radiation with a germanium monochromator operated at 35 mA and 35kV. The data collections were done in the 2θ range of 5-100^o with 0.005^o increments. The preliminary analysis were done by using STOE WinXPOW [56] and Inorganic Crystal Structure Database (ICSD) [57].

Besides, in the XRPD diffractograms of the all samples, two very weak reflections can be observed at $2\theta \approx 17.5°$ and 21° which is due to the Mylar® Polyester films.

2.3.2. Differential Thermal Analysis / Thermal Gravimetry

In order to study the thermal behavior of the as-prepared (dried) samples, thermogravimetric and differential thermal analysis measurements (DTA/TG) were performed using DTA/TG Seiko SSC 5200 model apparatus. The heating rate of the sample was 10 K/min under air and CO_2 free synthetic air. For the preparation of samples, approximately 10 mg of finely ground samples was loaded into aluminum oxide (Al_2O_3) crucible. Data manipulations and analysis were performed with the software EXSTAR6000.

2.3.3. Mass Spectroscopy

Gas mass analysis of evolved gases during the heat treatment of the samples in the DTA/TG chamber were carried out using a quadrupole mass spectrometer ThermoStar^{TM} GSD 301 T. DTA/TG and mass spectrometer was connected via capillary and worked simultaneously. Multiple Ion Detection (MID) program was used with the chosen mass channels of 18 ($H_2O^{\bullet+}$), 32 ($O_2^{\bullet+}$), 44 ($CO_2^{\bullet+}$). Ion currents of the selected mass channels are recorded versus time during the mass spectrometer measurements.

2.3.4. Infrared Spectroscopy

The Fourier transform infrared (FTIR) spectra were carried out a JASCO FT-IR 600 Spectrometer in the wavenumber region of 4000-400 cm^{-1} under nitrogen gas. All data manipulations were done by using JASCO Spectra Manager Software [58].

For the preparation of annealed samples potassium bromide (KBr) disc method was used. The specimens were prepared by mixing approximately 3 mg finely ground compound with 300 mg of dried powder KBr and then pressed in a die under approximately 8 tons of pressure for 5 minutes to make a pellet of 13 mm diameter.

2.3.5. High Resolution Transmission Electron Microscopy

High resolution transmission electron microscopy (HR-TEM) investigations were carried out with a Philips CM 200 FEG at an acceleration voltage of 200 kV by Dr. Wilder Carrillo-Cabrera from Max Planck Institute for Chemical physic of solids, Dresden-Germany. TEM images were processed by Digital Micrograph (Gatan, USA).

2.3.6. Dynamic Light Scattering

The particle sizing measurements were performed by a dynamic laser light scattering (DLS) technique, using a Zetasizer Nano ZS (Malvern Instruments). The excitation source was a 4 mW He–Ne laser emitting at a wavelength of 633 nm in linearly polarized single-frequency mode, which was focused onto the sample cell. Scattered light obtained from the samples kept in a 5 ml quartz cuvette was detected by a photomultiplier tube. For the measurements of the particle size and size distribution, the powder of rare earth oxides was dispersed in DEG-TEG polyol mixture and obtained transparent solutions were measured at room temperature (298±2 K).

Chapter 3

RESULTS & DISCUSSION

3.1. Nano-Sized Rare Earth Oxides

3.1.1. Nano-Sized Rare Earth Oxides Prepared via Liquid Crystal Templating Method

3.1.1.1. Thermal Decomposition Analyses

The thermal behavior of the as-prepared samples was investigated by DTA/TG measurements and the phase transformation temperatures, appropriate conditions for sample annealing for oxide formation were determined. In addition, to identify the gasses liberated, mass spectroscopy provided information. The exothermic and endothermic effects were connected to the possible reactions, phase transformations and temperatures where they take place were determined during the heat treatment. The results were also compared with XRPD data.

All as-prepared samples prepared from $RE(NO_3).nH_2O$ (n = 4-6; RE = Pr, Nd, Sm, Eu, Gd, Dy, Ho, Er, Tm, Yb, Lu) had the same thermal behavior under air atmosphere. During the heat treatment, the first broad endothermic peak between 300 K and 500 K can be assigned to chemisorbed and physisorbed water. Increasing the temperature further the organic component decomposed to CO_2. Finally, at around 723 K, they transformed completely into pure oxides.

Because all as prepared sample showed similar behavior (except neodymium), europium was chosen to show the characteristic behavior in details. TG/DTA analysis and mass spectroscopy results under air atmosphere during the thermal treatment are depicted in Fig. 3.1. DTA curve indicates that Eu sample transformed completely to Eu_2O_3 through one main exothermic weight loss process. TG curve exhibits the first weight loss step between 293 and 500 K which is attributable to the dehydration of water and is proved by the water signal (*m/e* = 18 in Fig. 3.1) in the mass spectra (MS) in the temperature range 250 - 450 K. The main weight loss step between 500 and 700 K in TG curve was due to condensation of the hydroxide sample and removal of the surfactant Brij56® which were left in the sample after washing with ethanol/diethyl ether mixture. Between this temperature ranges, the exothermic peak near 560 K can be accompanied with the oxidative decomposition of the surfactant. Fig. 3.1 also shows that simultaneous consumption of gaseous oxygen (*m/e* = 32) occurring at around 530 K which can be the indication of the oxide formation as well. The evolution of H_2O (*m/e* = 18) and CO_2 (*m/e* = 44) was attributed to the decompositions of the surfactant. In these temperatures, europium hydroxide sample formed mainly oxides. However, pure europium oxide formation occurred at around 723-748 K.

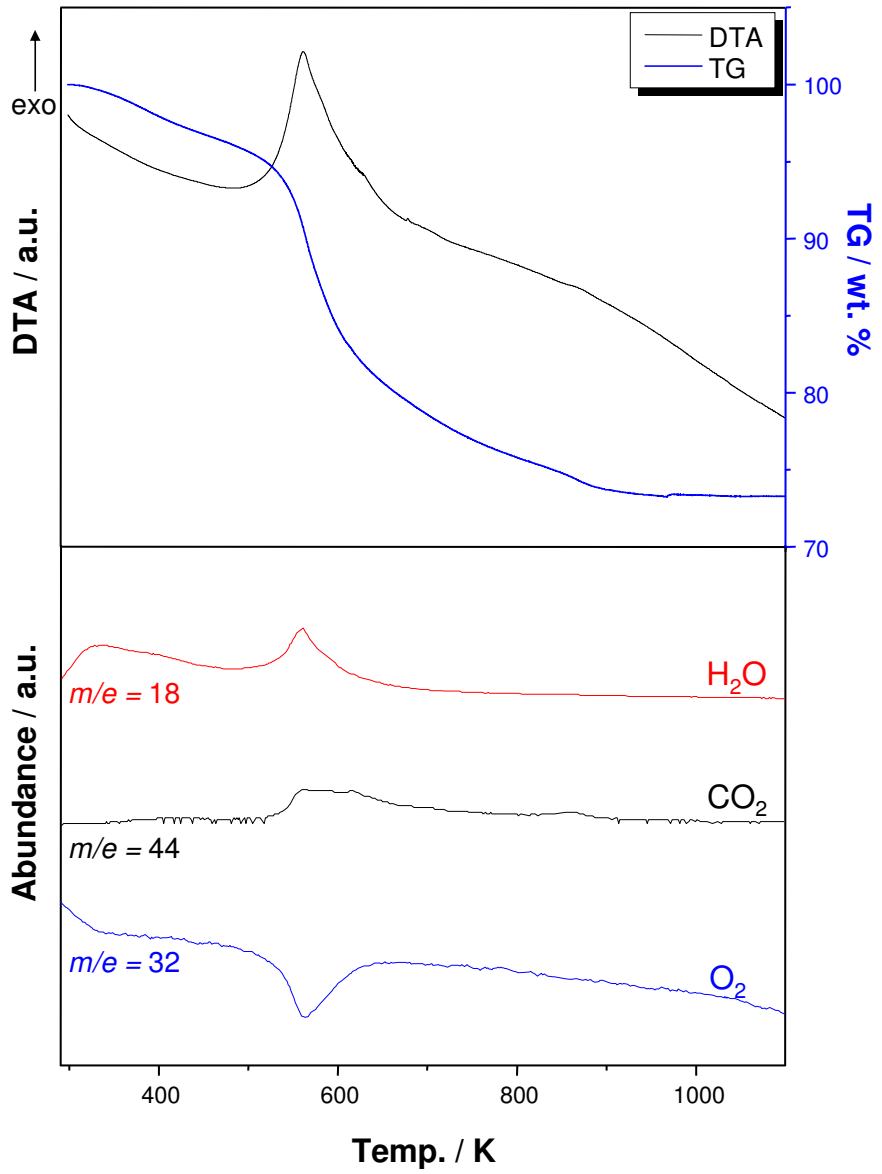

Fig. 3. 1 DTA-TG curve for as-prepared sample of europium under synthetic air and mass spectra (MS) of characteristic ions (*m/e*) for gaseous products liberated during the thermal decomposition.

Unlike other as-prepared samples, neodymium sample showed different thermal behavior during the heat treatment. Fig. 3.3 shows the DTA/TG graph together with mass spectra of gaseous products liberated taken on neodymium as-prepared sample in air. $Nd(OH)_3$ sample decomposed to Nd_2O_3 through three weight loss steps in air. The weight loss up to 500 K was mainly due to phase transition from $Nd(OH)_3$ to $Nd(CO_3)OH$ with simultaneous consumption of gaseous CO_2. The evolution of H_2O, in this temperature range, was basically attributable to the dehydration of surface absorptive water of the sample. Fig. 3.3 indicates that, upon further heating, between the temperature range of 500-800 K, carbonate hydroxide phase of neodymium decomposed to neodymium oxide carbonate, $Nd_2O_2CO_3$, with liberating H_2O and CO_2. This formation was approved by XRD diagram showed in Fig. 3.8. Between this temperature range, DTA curve exhibits a dominant exothermic peak centered at 550 K. Overall reactions taking place during phase transformation from $Nd(OH)_3$ to $Nd_2O_2CO_3$ can be shown as follows:

$$Nd(OH)_3 + CO_2 \rightarrow Nd(CO_3)OH + H_2O_{(g)} \qquad \text{(eq. 3.1)}$$

$$2\ Nd(CO_3)OH \rightarrow Nd_2O_2CO_3 + H_2O_{(g)} + CO_{2(g)} \qquad \text{(eq. 3.2)}$$

The phase, $Nd_2O_2CO_3$, remained stable up to 880 K and decomposed completely to Nd_2O_3 with CO_2 evolution in air. The XRD diagram of the $Nd_2O_2CO_3$ heated at 900 K which proves the formation of Nd_2O_3 is shown in Fig. 3.2. This decomposition process can also be identified with the small endothermic peak in the DTA curve.

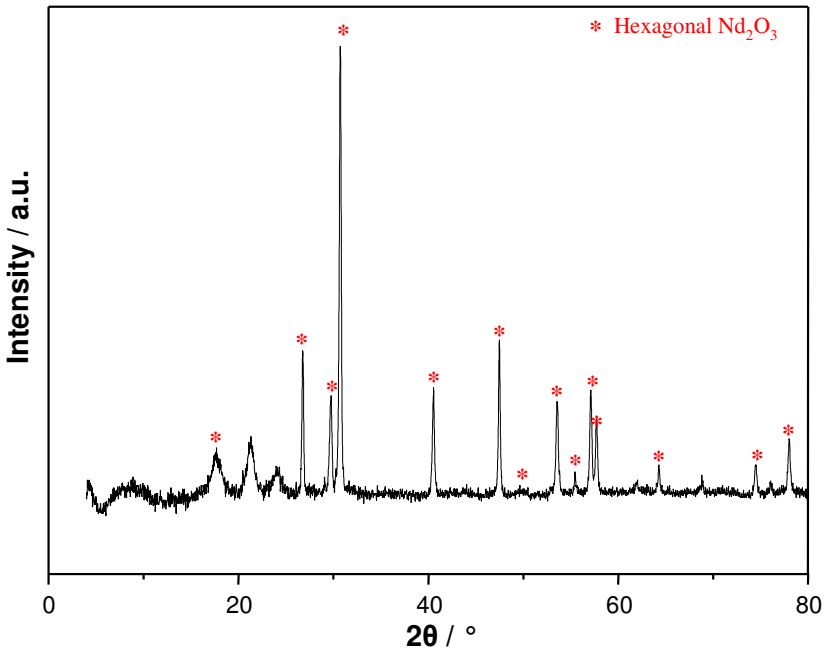

Fig. 3. 2 XRD diagram of $Nd_2O_2CO_3$ heated at 900 K for 4 h under air

However, when the thermal decomposition analysis was repeated in synthetic air, the as-prepared sample of neodymium decomposed gradually to pure Nd_2O_3. Similar to the thermal behavior of the remaining rare earth samples, neodymium sample first lost the surface absorbed water in the temperature range of 300-480 K as shown in Fig. 3.4. The evolution of H_2O in the MS curve was observed in the corresponding temperature range. Further heating resulted decomposition of the sample and oxidative decomposition of surfactant in 480-680 K range. This process was connected with the consumption of O_2 and evolution of H_2O and CO_2, respectively.

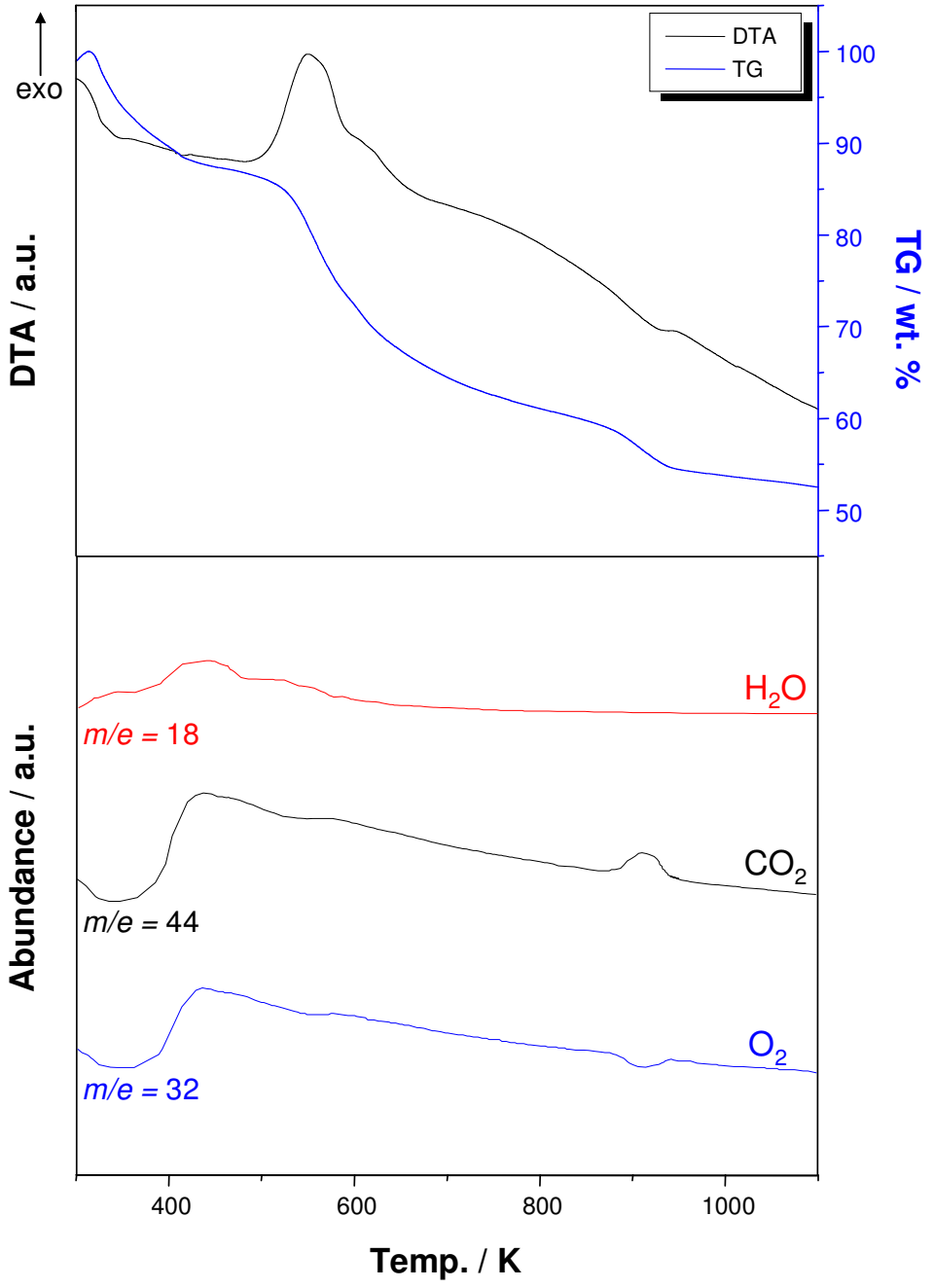

Fig. 3. 3 DTA-TG-MS curves for as-prepared sample of neodymium under air

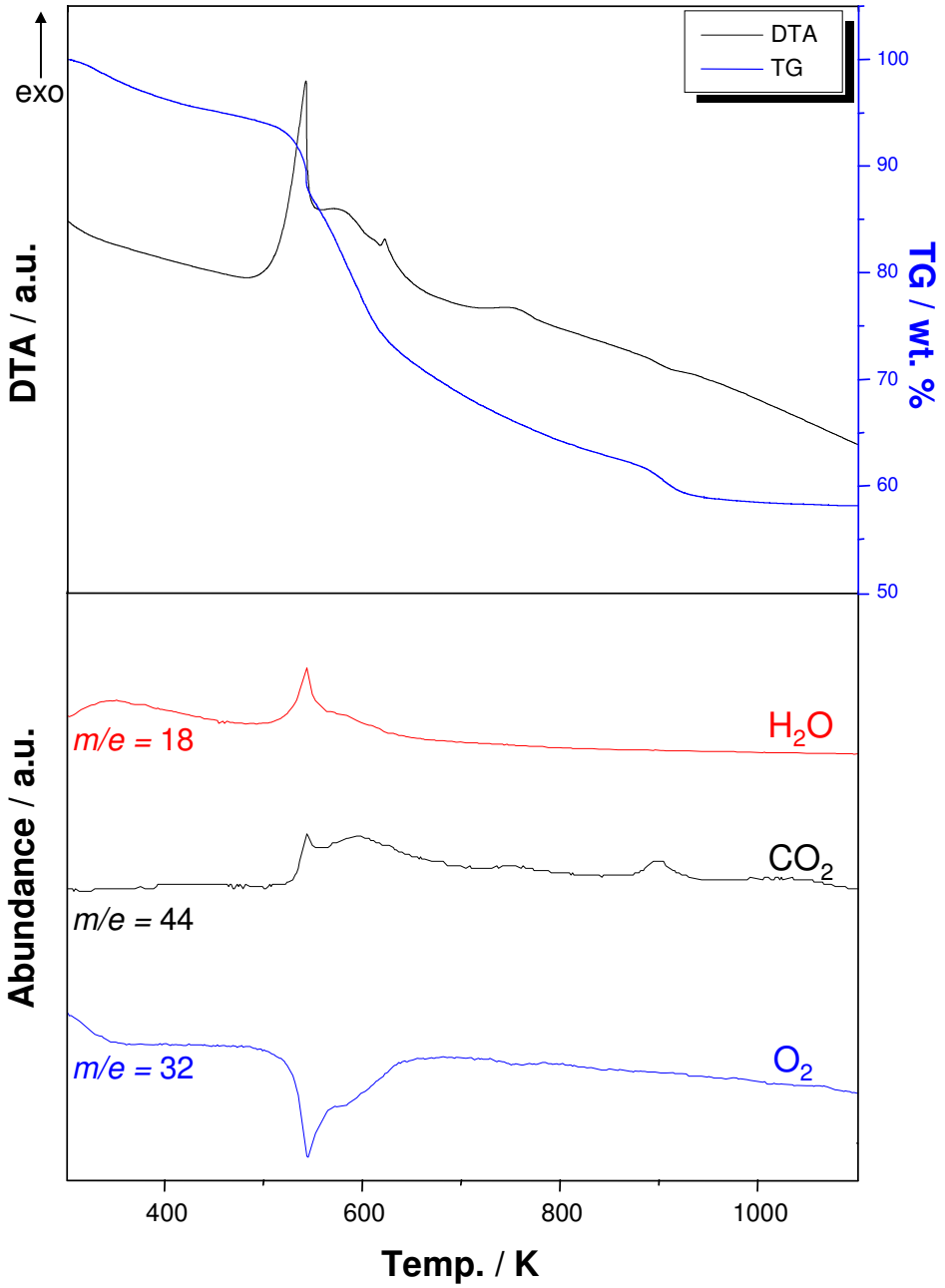

Fig. 3. 4 DTA-TG-MS curves for as-prepared sample of neodymium under synthetic air

3.1.1.2. XRD Analyses

XRPD measurements were performed for all as-prepared and annealed samples to characterize the formed structures, investigate their compositions, their phase transformations and calculate the grain size of their final products. The XRPD results show that as-prepared samples have similar structures with nearly the same reflection positions probably due to their very close atomic radius values. In Fig. 3.5, XRD diagrams of selected as-prepared samples are presented. They consisted of predominantly hydroxides of rare earth metals. However, as rare earth hydroxides formed in nano-sizes with disordered-amorphous structure, they gave weak reflections in the XRPD diffractograms. In fact, parts of reflections matched with rare earth hydroxide nitrates and hydroxide carbonate reflections.

The intense and broad reflections in the $2\theta \approx 10^{o}$ observed in XRPD diffractograms of as-prepared samples were probably coming from the surfactant.

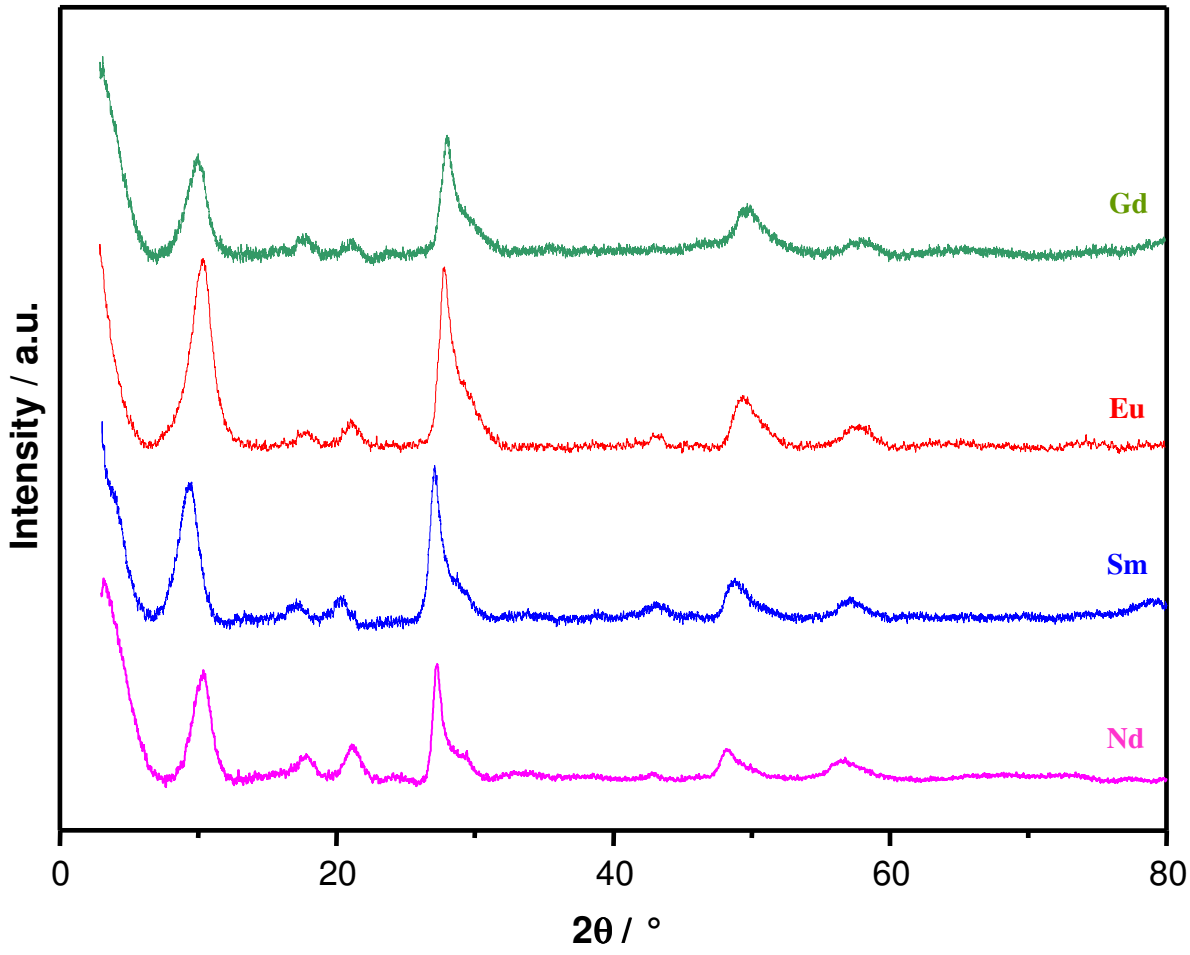

Fig. 3. 5 XRD diagram of $RE(NO_3)_3$ / surfactant mixture after NH_3 gas treatment (as-prepared) (RE: Nd, Sm, Eu and Gd).

To better define the composition of the as-prepared samples, neodymium sample was heated at 623 K for 12 h under oxygen atmosphere. According to the DTA result of as-prepared sample in air (Fig. 3.1), no exothermic or endothermic peaks were observed before 700 K. Therefore, with the heat-treatment, the grain size of the as-prepared samples can be increased to get better reflections in the XRPD pattern. Fig. 3.6 shows the XRPD pattern of this product and confirms that it had only hexagonal Nd_2O_3 and $Nd(OH)_3$. Based on this fact, it can be concluded that as-prepared samples consist of predominantly rare earth hydroxides. The presence of rare earth oxide in the as-prepared sample was also confirmed by HR-TEM analysis (Chapter 3.1.1.4).

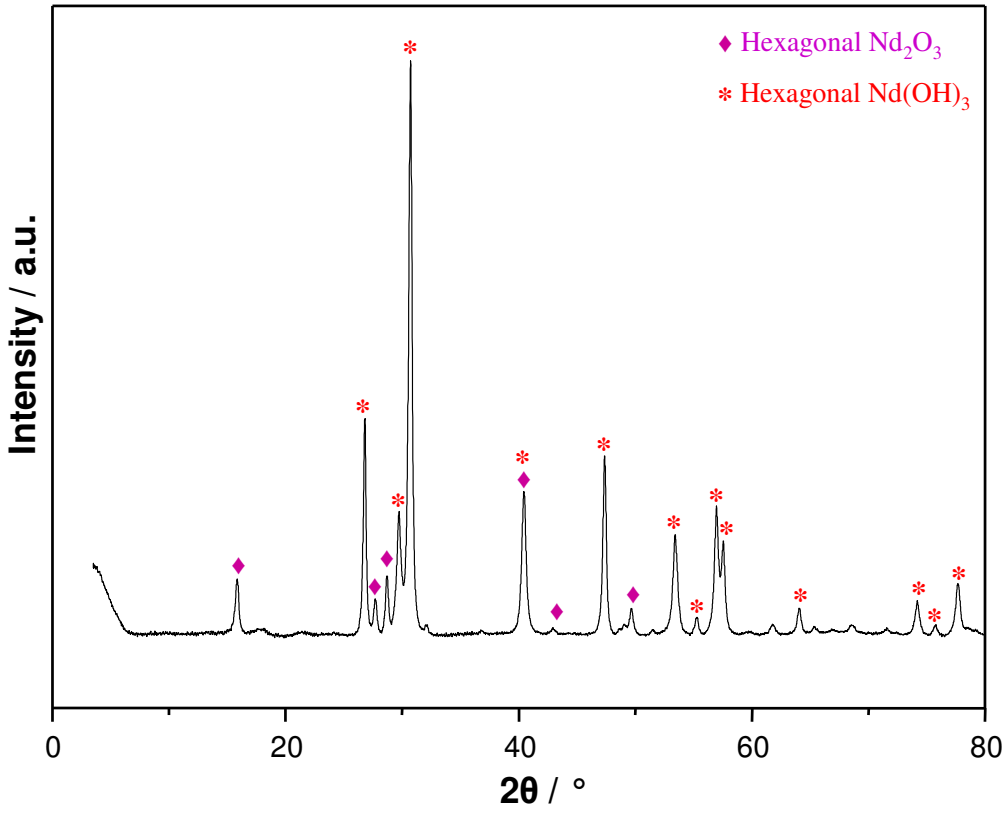

Fig. 3. 6 XRD diagram of neodymium sample heated at 623 K for 12 h under oxygen atmosphere

Moreover, the DTA/TG results reveal that neodymium as-prepared samples showed different thermal behavior depending on atmospheric environment during the heat treatment (Fig. 3.3 and Fig. 3.4). All of the as-prepared samples, except neodymium one, formed RE_2O_3 around 723-773 K under air atmosphere. Indeed, XRPD diffractograms confirm that after annealing at 773 K under air atmosphere, as-prepared samples formed pure RE_2O_3. The XRD diagrams of selected as-prepared samples of Eu and Er after being annealed are given in Fig. 3.7.

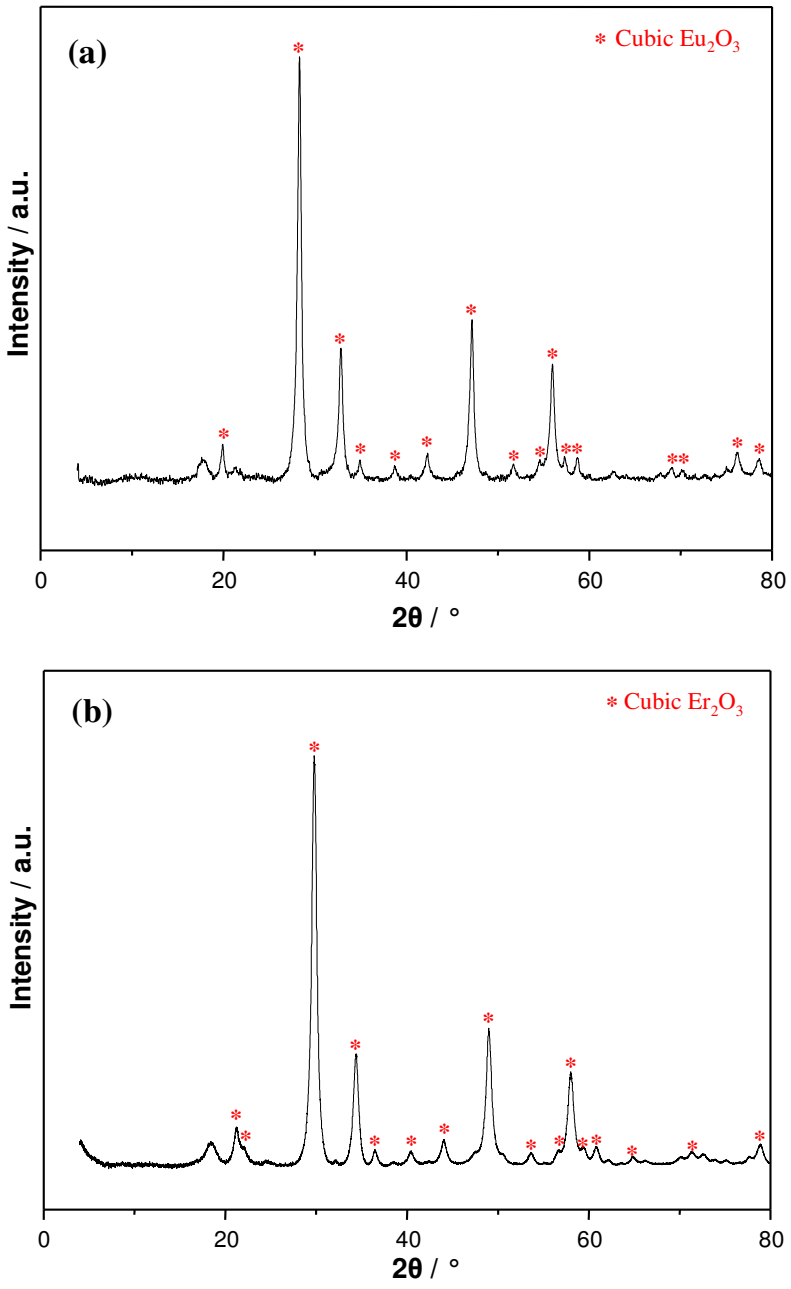

Fig. 3. 7 XRD diagrams of (a) europium and (b) erbium as-prepared samples heated at 773 K for 24 h under air atmosphere

In the case of neodymium samples, although they were mainly composed of neodymium hydroxide in their intermediate phases, according to the MS curve of the sample in air, they absorbed CO_2 from air (Fig. 3.3) and formed unstable neodymium carbonate hydroxide hydride, $Nd_2(CO_3)(OH)_4$ during the heat treatment under air atmosphere. Fig. 3.8 reveals that further heating induced phase transition from carbonate hydroxide to oxide carbonate, $Nd_2O(CO_3)_2$. The DTA/TG curve of neodymium sample in air shows that this product was stable up to 973 K and after this temperature it decomposed completely to Nd_2O_3 (Fig. 3.2). In contrast to air atmosphere, under CO_2 free air synthetic air, neodymium samples directly decomposed to hexagonal Nd_2O_3 at 773 K similarly to the other samples (Fig. 3.9).

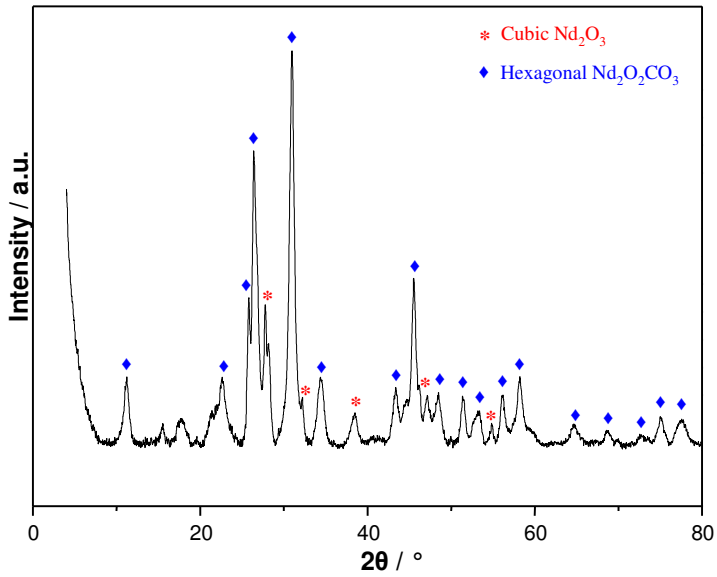

Fig. 3. 8 XRD diagram of neodymium sample annealed at 773 K for 24 h under air atmosphere

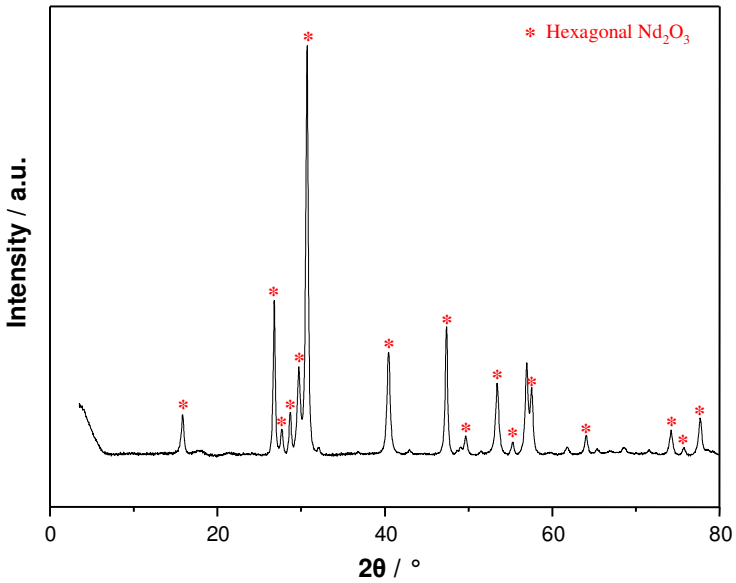

Fig. 3. 9 XRD diagram of neodymium sample annealed at 773 K for 24 h under synthetic air atmosphere

3.1.1.2.1. Particle Size and Grain Size Calculations

The average particle size, D_v, of the materials can be calculated by applying Debye-Scherrer's equation on XRD diagrams. The Debye-Scherrer's equation is

$$D_v = \frac{K\lambda}{B\cos\theta_B} \qquad \text{(eq. 3.3)}$$

where λ is the X-ray wavelength, B is the full width of height maximum (FWHM) of a main diffraction peak, θ_B is the diffraction angle, and K is the Scherrer constant. With these equation, the average crystalline grain size of a material having particles smaller than 100 nm can be calculated [59, 60]. The calculated average grain sizes of the annealed samples are given in Table 2. The particle sizes measured by DLS were bigger than the sizes calculated from Debye-Scherrer's equation, indicating that the obtained rare earth oxides were agglomerated.

Table 2 Calculated average crystalline grain size (D_v) and measured particle size (d) of the samples after being annealed at 773 K for 24 h

	Pr_2O_3	Nd_2O_3	Sm_2O_3	Gd_2O_3	Dy_2O_3	Er_2O_3	Tm_2O_3	Yb_2O_3
D_v (nm)	13	10	23	11	9	11	12	10
d (nm)	47	29	92	66	36	24	44	45

3.1.1.3. Fourier Transform Infrared Analysis

The interactions between surfactant, Brij56®, and rare earth salts were investigated on a molecular level through the use of Fourier transform infrared (FTIR) spectroscopy. In FTIR, resonant frequencies are related to the strength of the bonds and the mass of the atoms. As rare earth metals have very close molecular weights, their effects on the bond strength of the surfactant molecules are very similar. For this reason, the entire as-prepared samples had similar spectra. Fig. 3.10 shows the FTIR spectra of the selected samples. To explore the surfactant/inorganic interaction and the mechanism of self-assembly into liquid-crystalline phase, europium as-prepared sample was investigated. Fig. 3.11 shows the FTIR spectra of the as-prepared sample of europium and surfactant. Appearance of absorption band in the FTIR spectrum of the surfactant at 3445 cm^{-1}, shown in Fig. 3.11(b), was corresponding to O-H stretching, which was due to the presence of OH group of the surfactant. The sharp peaks observed at 2952 and 2922 cm^{-1} could be assigned to C-H bond stretching. Compare to the FTIR spectrum of surfactant, the O-H stretching and bending vibrations at 3445 and 1592 cm^{-1} showed significant increase in the FTIR spectrum of the as-prepared sample, shown in Fig. 3.11(a), suggesting that O-H was coming from the $Eu(OH)_3$. Furthermore, the C-O stretching vibrations of the ethylene oxide groups of surfactant at 1114 cm^{-1}, undergoes red-shift to 1105 cm^{-1}. This peak originating from the C-O stretching modes of the ethoxide group of the surfactant coordinated to the Eu^{3+} ion of the as-prepared samples. This is a good indication of the strong interactions between hydrophilic ethylene oxide chain of the surfactant and the rare earth salts.

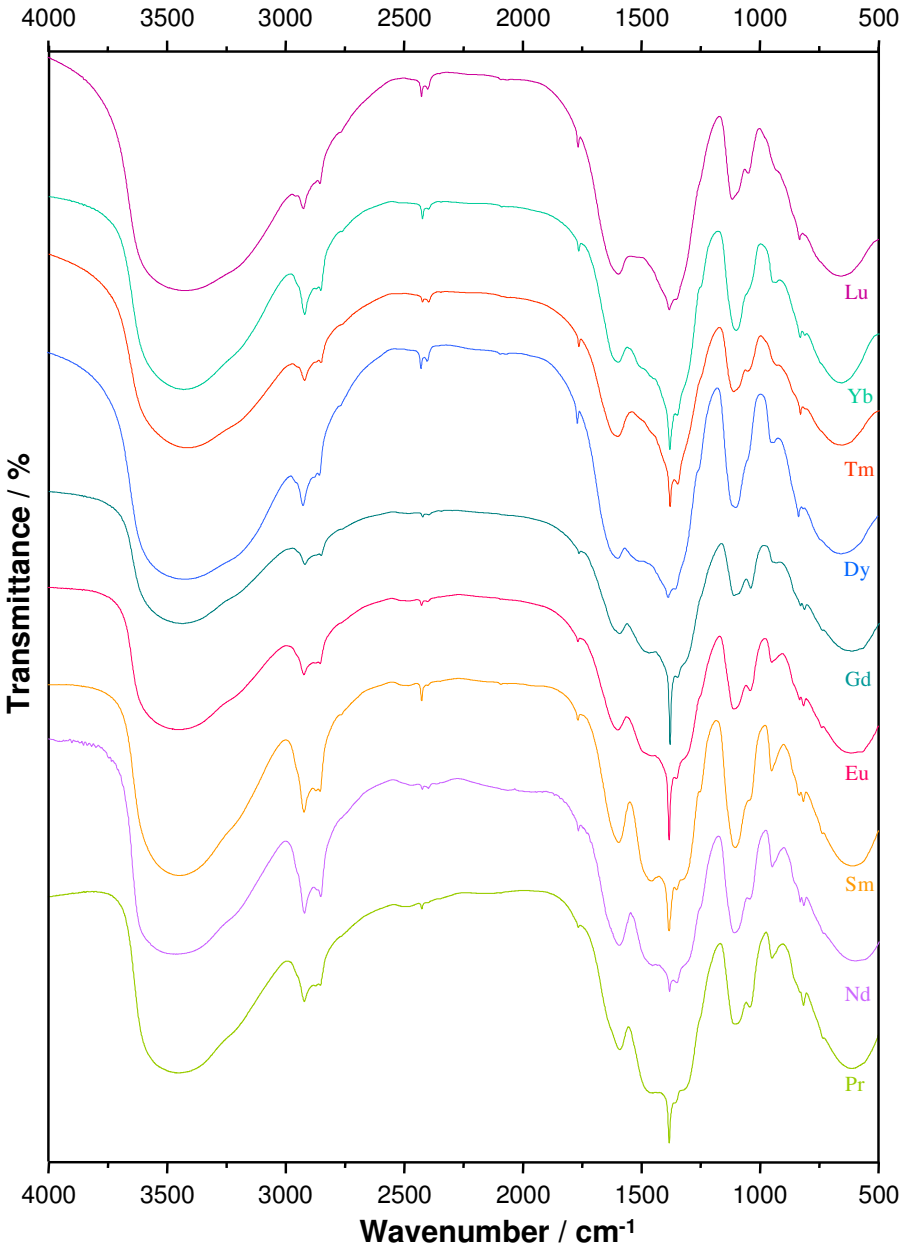

Fig. 3. 10 FTIR spectra of as-prepared samples

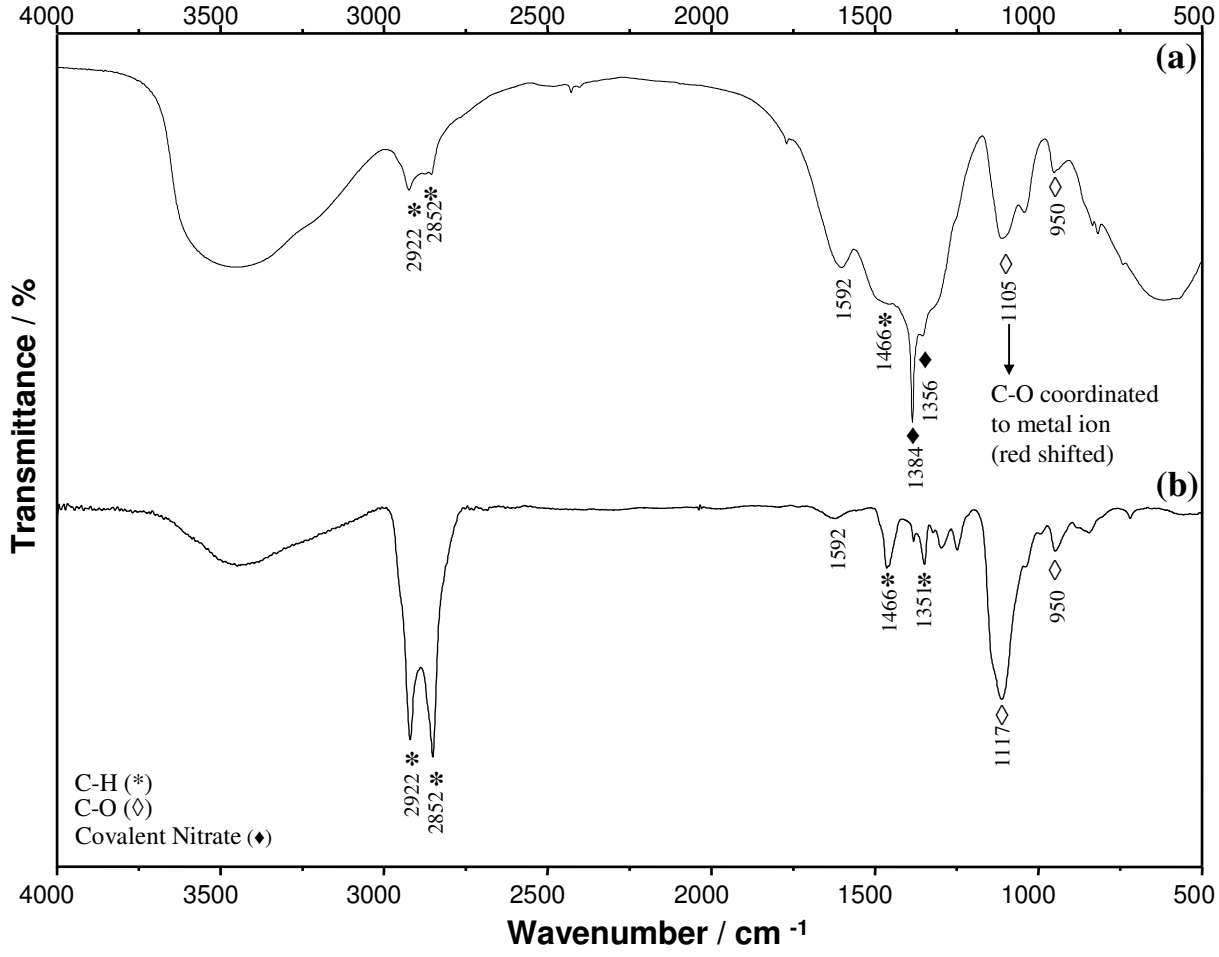

Fig. 3. 11 FTIR spectrum of the as-prepare sample of (a) europium and (b) pure Brij56®

Surfactants are organic molecules which comprise at least one hydrophilic head group and one hydrophobic tail group [61, 62]. Because of such molecular structure, surfactants are able to be absorbed to the surface or interface of the inorganic nanoparticles and reduce the surface energy even when they are in present at a low concentration. The major driving forces for the surfactants to self-assembly into complex structures are enthalpically unfavorable interactions: the hydrophobic attractions at the hydrocarbon– water interfaces and the hydrophilic ionic or steric repulsion between the head groups are the competing forces.

The surfactant used for the preparation of nano-sized rare earth oxides is oligo(ethylene oxide) type non-ionic surfactant, dodecyl(ethylene oxide), $C_{12}H_{25}(CH_2CH_2O)_{10}OH$. The interaction between the surfactant head group and water molecules of precursor induce the surfactant/inorganic mesostructure. The ethylene oxide chain of the surfactant form reverse micelle structures on hydrous rare earth salts. Because of the repulsive interaction between the head group and tail group, the head group and the salt are located in the micelle core and the hydrophobic groups extend away from the center forming the reverse micelles. According to FTIR results, it is proven that the intermolecular forces between the inorganic precursor and the surfactant are hydrogen-bonding (Fig. 3.11). Fig. 3.12 illustrates the schematic representation of the rare earth salt/surfactant mesostructure formation.

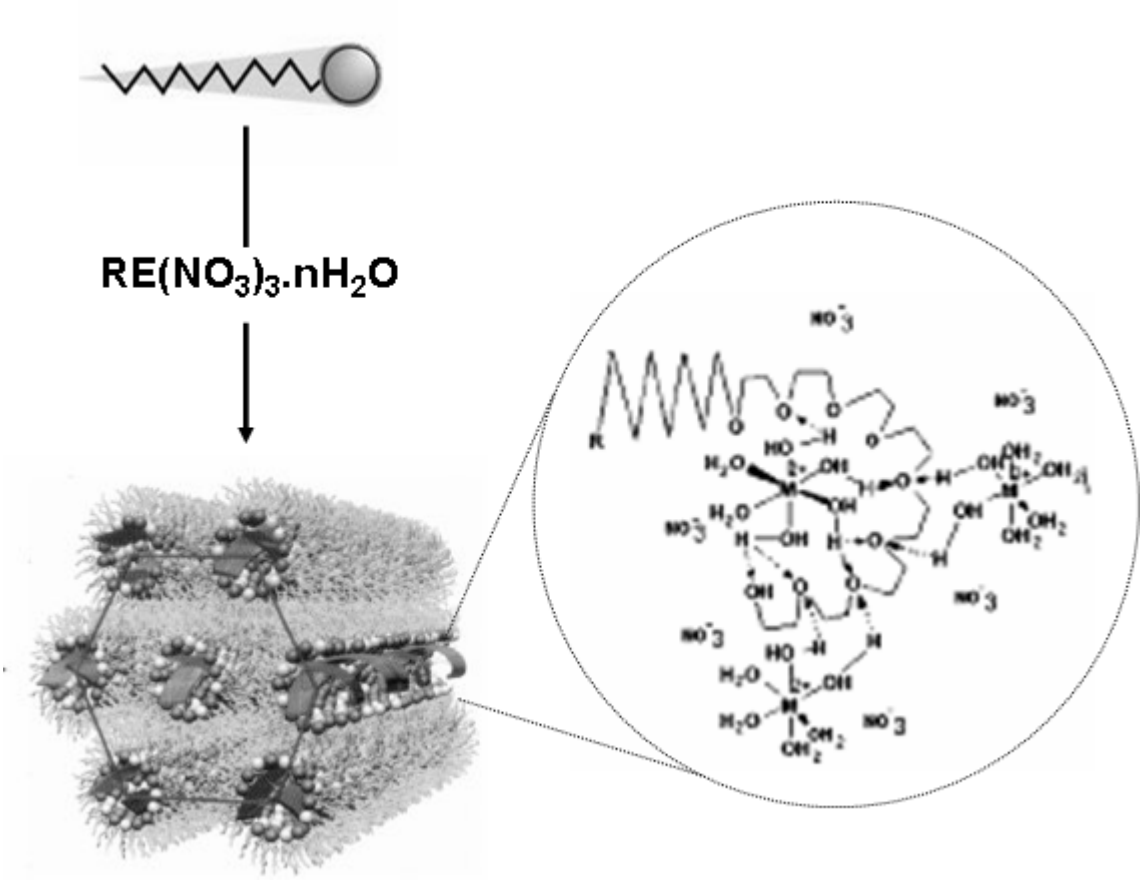

Fig. 3. 12 Schematic representation for the mechanism of the Brij56® self-assembly and the rare earth salt/surfactant mesostructure formation

3.1.1.4. High Resolution Transmission Electron Microscopy Analysis

The morphology and the structure evolution of the all samples were determined by HR-TEM. The Fast Fourier Transform (FFT) images from HR-TEM micrographs revealed that the as-prepared samples consist of rare earth oxides. Because all as prepared samples showed similar results, erbium and neodymium were chosen to show the characteristic behavior in details. In Fig. 3.13, different views of as-prepared sample of erbium are presented. As shown in Fig. 13(a), as-prepared sample consisted of large agglomerates built up from nanoparticles of Er_2O_3, this can be observed on the carbon support and shown in Fig. 3.13(b). Fig. 3.13(d) is FFT image of the Fig. 3.13(c). Although intermediate phase shows distorted structure, Fig. 3.13(d) confirms the existence of cubic Er_2O_3.

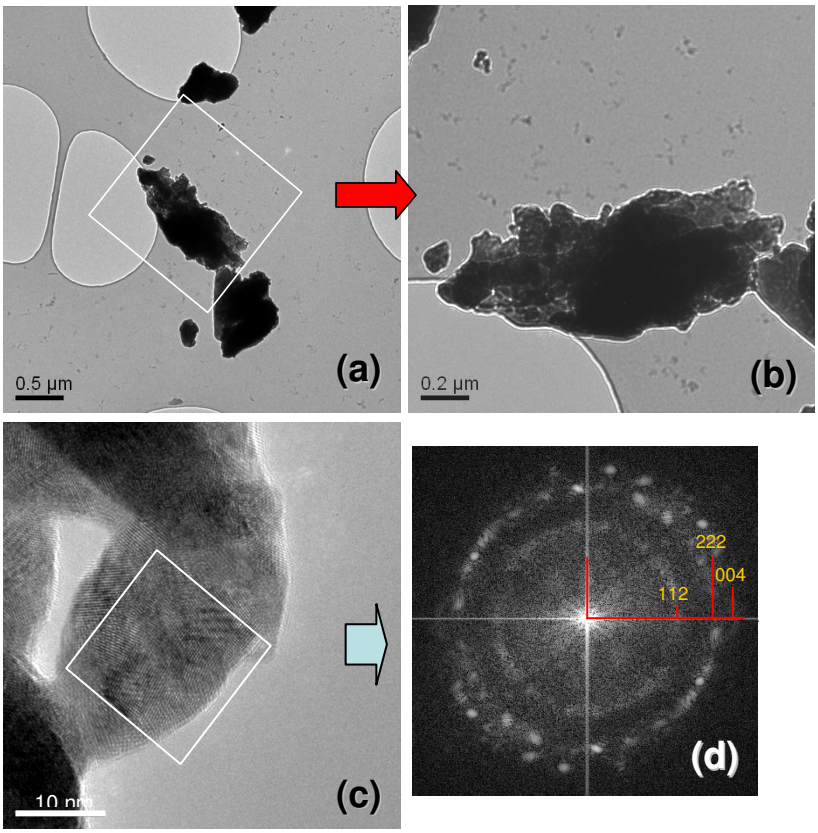

Fig. 3. 13 (a-c) HR-TEM images of as-prepared sample of erbium and (d) FFT image of (c)

After annealing in air atmosphere at 773 K, erbium sample preserved its rounded crystalline shape (Fig. 3.14(a)) and its cubic oxide structure (Fig. 3.14(d)). The average particle size of annealed Er_2O_3 was in the range of 7 to 12 nm, which is consistent with the calculated particle size.

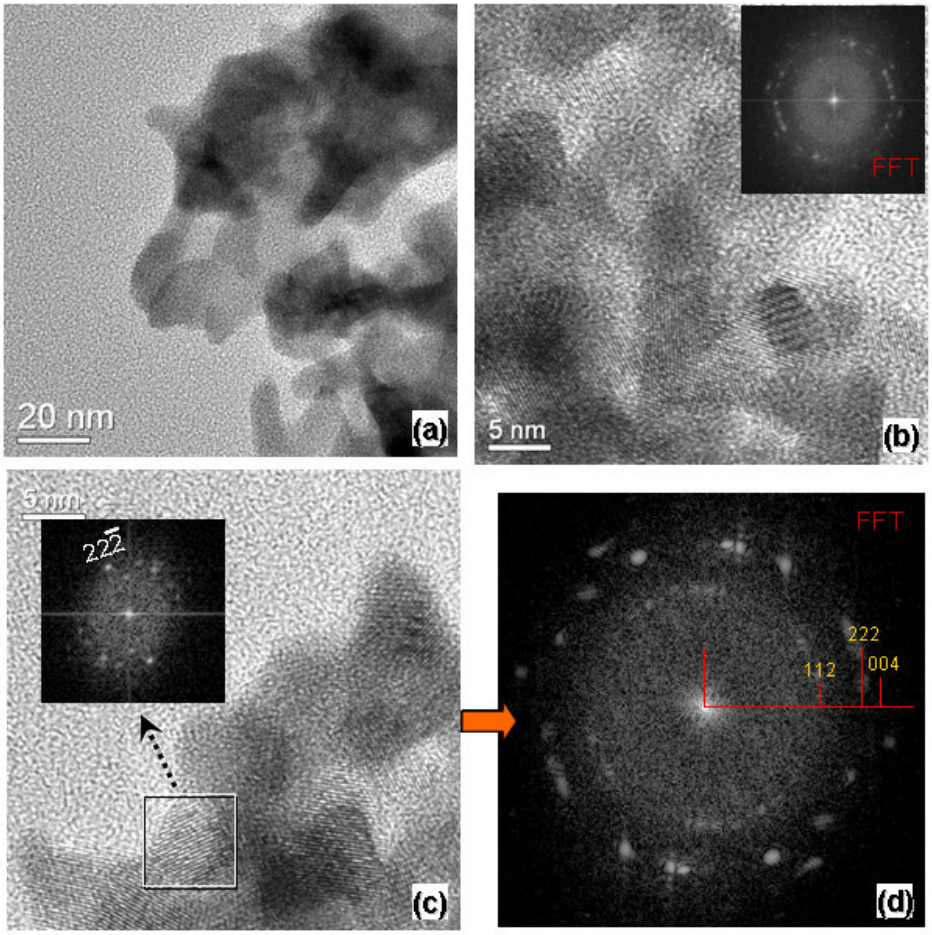

Fig. 3. 14 (a-c)HR-TEM images of annealed erbium sample and (d) FFT image of (c)

HR-TEM micrographs confirm that crystal structure of both final and as-prepared samples of rare earth oxides were cubic as observed in their bulk oxides. In contrast, crystalline structure of as-prepared samples of neodymium differed from its final product. The neodymium sample had trigonal structure (Fig. 3.15(b)), whereas final product, annealed at 773 K under synthetic air, had hexagonal structure (Fig. 3.14(c)). Fig. 3.14(a) shows that the neodymium as-prepared sample yielded distorted porous structure. Heating at 773 K under synthetic air atmosphere leaded to phase transformation from trigonal structure to hexagonal structure having low ordered porous structure. The average particle size of the annealed neodymium sample is 9 to 15 nm, which is consistent with the calculated particle size from Debye-Scherrer's equation.

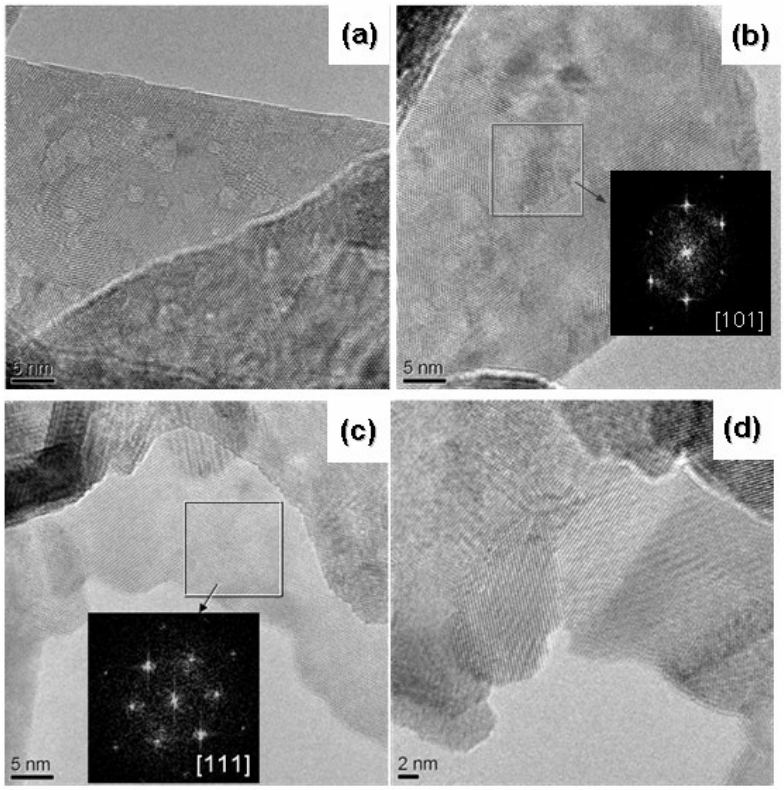

Fig. 3. 15 HR-TEM images of (a,b) the neodymium samples: as-prepared and (c, d) annealed

HR-TEM analysis shows that all as-prepared and annealed rare earth samples have disordered porous structures. Indeed, compared to annealed ones, as-prepared samples reveal much more disordered structures, and they have more surface-activity. From the HR-TEM images, the average particle sizes of the annealed samples are found to be ranging from 7 to 30 nm, which is in good agreement with the calculated ones from XRD patterns.

3.1.2. Nano-Sized Rare Earth Oxides Prepared via Sol-Gel Method

Thermal decomposition process of the europium, gadolinium and erbium samples prepared via sol-gel method was investigated by DTA-TG and MS analyses. As all there samples possessed similar behavior, europium sample was chosen for analysis. In Fig. 3.16, DTA-TG-MS profiles of the europium sample are given. The TG curve exhibits a slight decrease below 515 K which was due to removal of surface absorbed water. This slight weight loss in TG curve was also evidenced by the evolution of H_2O in the MS curve. Main transformation of europium sample started at about 530 K and proceeded as a two step weight loss process. The main weight loss step in the TG curve in the temperature region of 530 and 560 K indicates that organic residual of DEG and TEG dissociated at this temperature region. This weight loss step was accompanied with the sharp exothermic peak at 557 K with simultaneous consumption of O_2 and evolution of H_2O and CO_2. Further heating resulted in complete transformation of the as-prepared sample to Eu_2O_2.

As in thermal behaviors of the three samples, the samples had similar spectra. Fig. 3.17(a) shows the FTIR spectra of the europium as-prepared sample, annealed sample and pure DEG-TEG mixture in the spectral region 2700-3700 cm^{-1}. The spectra demonstrated that the asymmetric and symmetric C-H stretching vibrational bands at ~2850 cm^{-1} and ~2920 cm^{-1}, respectively, disappeared after annealing the sample in air at 773 K for 24 h. This suggests the complete removal of the organic solvent DEG-TEG mixture.

XRD pattern of the as prepared samples, which are not shown, revealed that they are amorphous and no diffraction peak could be observed. The oxide of europium, gadolinium and erbium can be obtained by annealing the as-prepared samples at 773 K. The XRD patterns of the annealed samples were shown in Fig. 3.17(b).

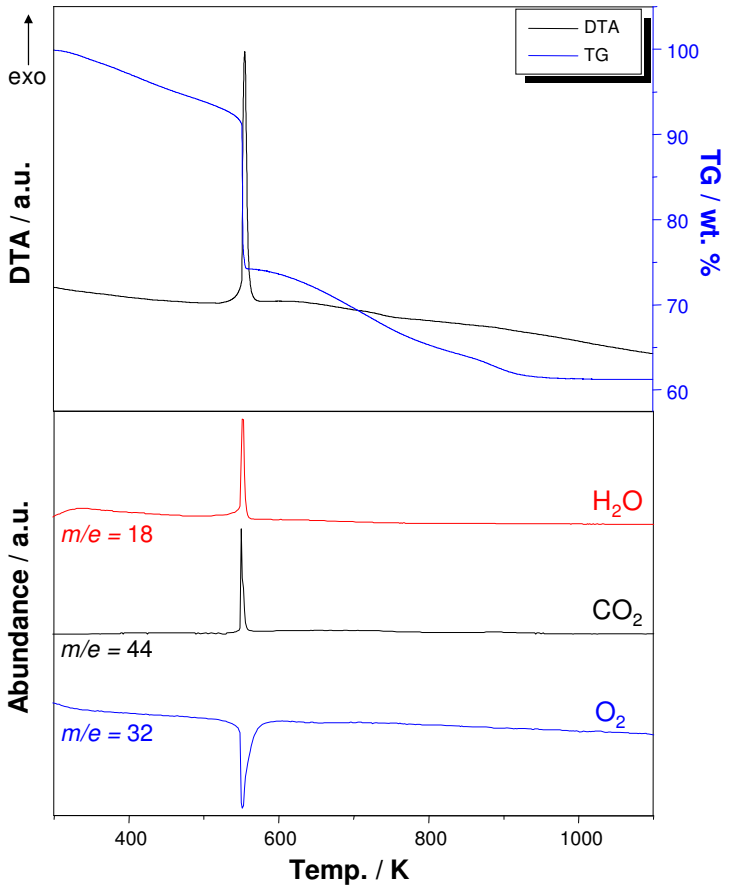

Fig. 3. 16 DTA-TG-MS curves for as-prepared sample of europium under synthetic air

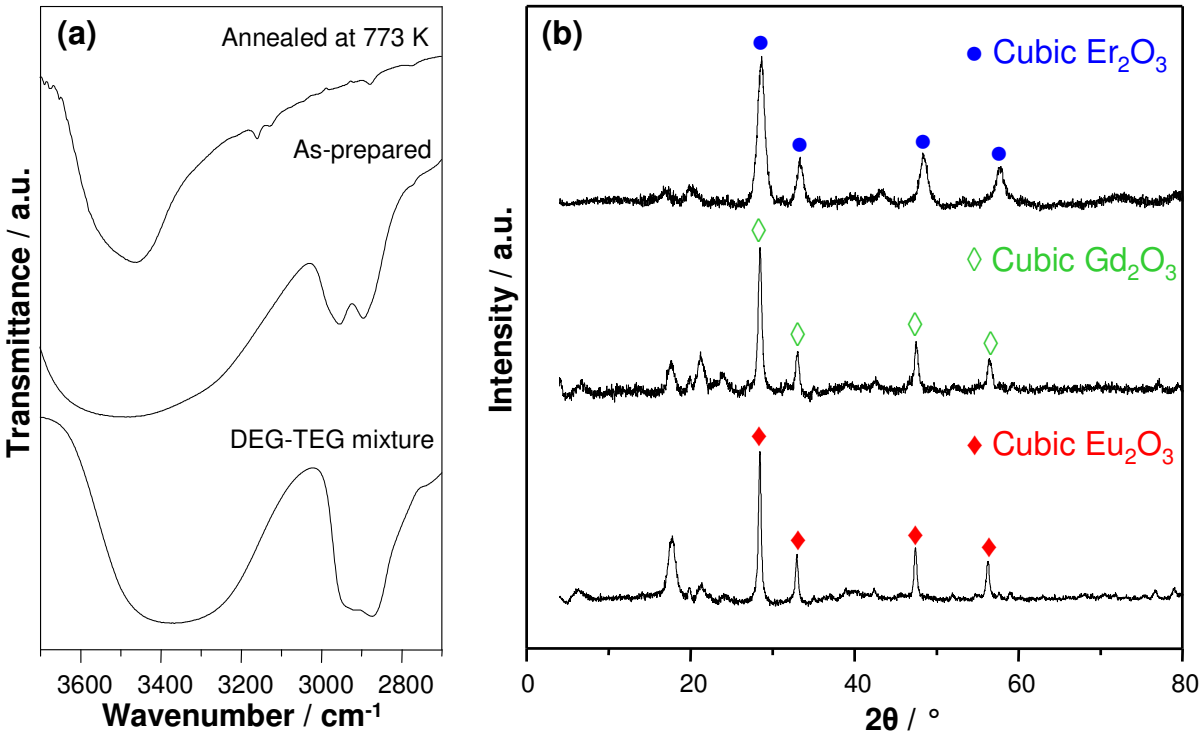

Fig. 3. 17 (a) FTIR spectra of as-prepared, annealed samples of europium and pure DEG-TEG mixture. (b) XRD patterns of the annealed samples

In contrast to liquid crystal templating method in which the stabilization of rare earth particles were achieved by the coordination of surfactant to the hydrous rare earth salts, in the sol-gel method, the precursor was hydrolyzed to form colloidal rare earth particles and the DEG-TEG polyalcohol mixture was surface absorbed by these particles. High viscosity of the polyalcohol mixture prevents the growth of rare earth particles by decaying the transport of ions and steric hindrance by the absorption of polyalcohol mixture on the surface of these particles hampers the particle-particle aggregation.

3.1.2.1. Light Emission in nano-sized Eu_2O_3 particles

This study was carried out with the collaboration of Photonic Crystal group in Instituted of Material Science, Madrid (CSIC). Nano-sized Eu_2O_3 particles prepared via sol-gel method was incorporated within the structure of artificial inverse opals to study the spontaneous emission of europium.

In particular, emission properties of the light emitting materials can be modified by nanostructuring. In this sense, photonic crystals have turned out to be an appropriate tool for inhibiting the emission of light [63]. Photonic crystals (PCs) are materials in which the refractive index is periodically modulated on a length scale comparable to wavelength of light. In other words, PCs are dielectric materials in which light of certain energies cannot propagate [64]. PCs exhibit bandgaps which prohibits light propagation in some defined directions. Therefore, overlapping bandgap with the emission bands of embedded luminescent europium will inhibit the emission of luminescent europium.

To embed the prepared Eu_2O_3 into Al_2O_3 inverse opals, the annealed particles were dispersed in the mixture of acrylic acid and water. The acrylic acid molecules were coordinated to Eu_2O_3 through their oxides and separated weakly agglomerated particles from each other. The monodisperse colloidal Al_2O_3 inverse spheres embedded with europium oxide complex were synthesized in two-step process. First, the colloidal films made of polystyrene (PS) microspheres were grown by the vertical deposition method [65]. Under appropriate conditions involving concentration and evaporation rate, closed packed monolayer of PS begin to grow at meniscus due to capillary forces. The diameters of the spheres were detected in order to match the bandgap of the inverse opal and the europium emission band. Micro-slides of glass were immersed in 0.15 vol. % aqueous suspension of microspheres. The sample was left undisturbed in 323 K oven until growth of the films was completed. SEM image of the prepared opals are given in Fig. 3.18(a). After synthesis of the bare opal, a thin layer of alumina (~15 nm) was deposited over each sphere of the opal

by atomic layer deposition (ALD). In order to remove PS and form the inverse opal, it was annealed at 723 K for 6 h and inverse opals were shown in Fig. 3.18(b). Finally, the sample was infiltrated with dispersed europium oxide by spin coating and Fig. 3.19 shows the sample infiltrated with Eu_2O_3. While bare inverse opals have green color, the infiltrated parts of the inverse opals have red color showing the successful infiltration of Eu_2O_3.

The sample was illuminated by 355 nm laser light and it exhibited red luminescence of Eu_2O_3. The photoluminescence spectrum of Eu_2O_3 embedded into opals is given in Fig. 3.20. Indeed, bandgap of Al_2O_3 inverse opals was matched with the emission bands of europium. However, study on lasing properties of the Eu_2O_3 particles on the basis of bandgap of opals is an on going project.

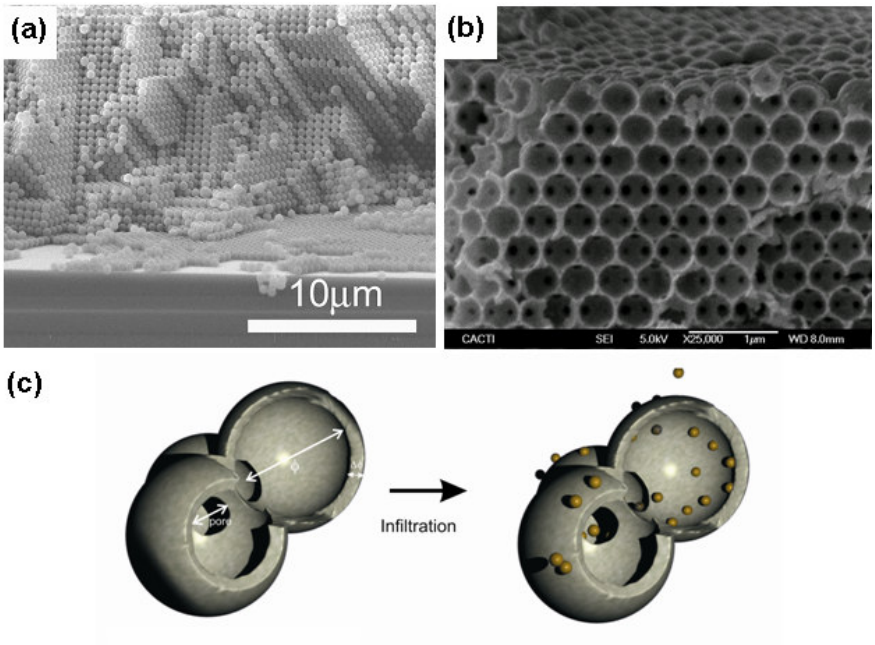

Fig. 3. 18 (a) SEM images of bare PS opals, (b) inverse Al_2O_3 inverse opals and (c) schematic representation of infiltrated inverse opals

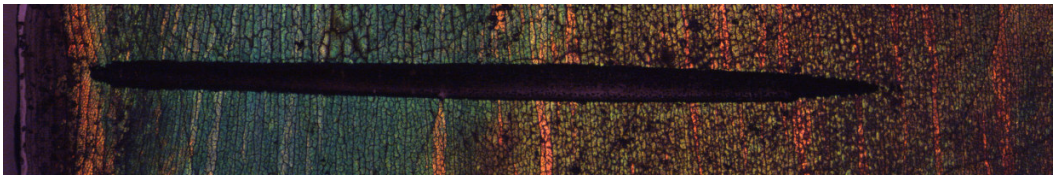

Fig. 3. 19 Optical microscopy image of the inverse Al_2O_3 inverse opals infiltrated with Eu_2O_3
(x20 magnified)

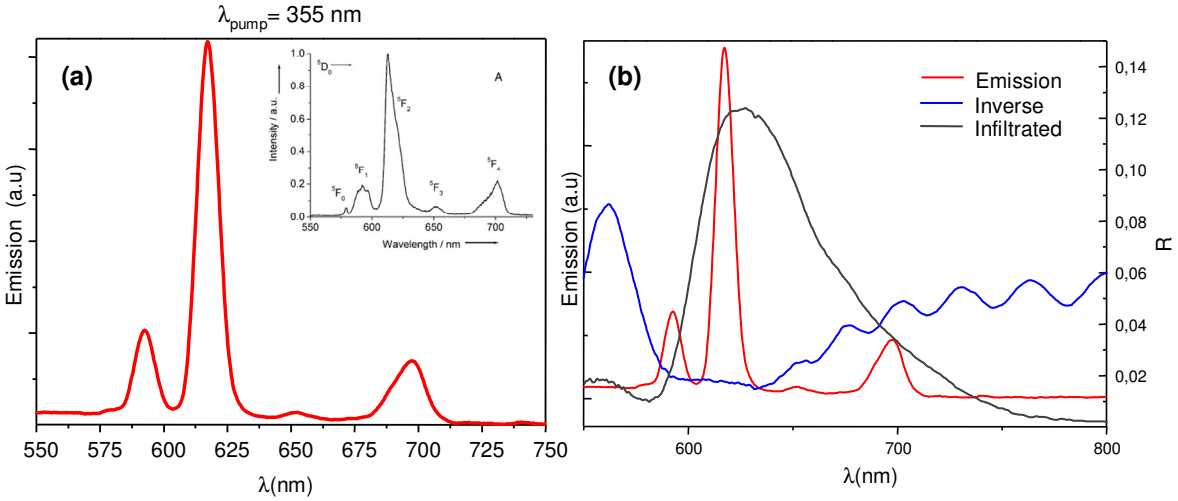

Fig. 3. 20 (a) Photoluminescence spectrum of Eu_2O_3 embedded in Al_2O_3 inverse opals and (b) reflectance spectra of inverse and bare opals with the emission of Eu_2O_3

3.2. Porous Zirconia

3.2.1 XRD Analyses

In order to investigate their phase developments and phase transitions with increasing annealing temperature, all as-prepared samples were annealed at 373, 723, 923 and 1123 K for 5 h. These temperatures were chosen based on DTA result (Fig. 3.23) where the curve has no exothermic at this temperature range.

The crystalline structure of zirconium oxide depends on the annealing temperature and it has three stable polymorphs: monoclinic (m-phase) below 1443 K, tetragonal (t-phase) between 1443 and 2643 K and cubic (c-phase) above 2643 K [66]. The t-phase has both acidic and basic properties, while it presents high strength and toughness. As a result, this phase gives the most active catalytic properties.

XRPD diffractograms of zirconium/Brij56® composites heat treated at four different annealing temperature are shown in the Fig. 3.21. The XRPD patterns illustrated that as-prepared samples, which were dried at 373 K, were amorphous. Crystalline zirconia with the mixture of m-phase and t-phase were formed after being annealed at 723 K. The diffraction patterns change as the annealing temperature increases. In the sample treated with $Zr(OC_2H_5)_4$ precursor, shown in Fig. 3.21 (b), transformation of the m-phase to the t-phase took place at 923 K, while in the sample treated with $ZrOCl_2.8H_2O$ precursor shown in Fig. 3.21(a), intensity of the main t-phase peak centered at 2θ ~30^o was increased indicating the rise of t-phase content. At 1123 K, the diffraction patterns of both samples were dominated by the characteristic peaks of the m-phase.

In comparison to the samples prepared with non-ionic surfactant, samples prepared with cationic surfactant CTAB formed crystalline zirconia with single t-phase after being annealed at 923 K, before this temperature both samples were amorphous as given in Fig. 3.22. The obtained t-phase was also stable up to 1123 K.

The results indicate that in the composites of zirconium/Brij56®, there were crystalline formation of the t- and m-phases, except for the composites with $Zr(OC_2H_5)_4$ precursor. However, the t-phase was only stable up to 923 K, increase in annealing temperature provoked transformation from this phase to the m-phase.

Stable t-phase of zirconia was obtained from the samples prepared with cationic surfactant CTAB. Furthermore, characterization with HR-TEM (Chapter 3.2.4) indicates that ordered porous structure was only obtained from the $ZrOCl_2.8H_2O$/CTAB composite. For these reasons, thermal and infrared spectroscopy analyses were performed only with the $ZrOCl_2.8H_2O$/CTAB composites.

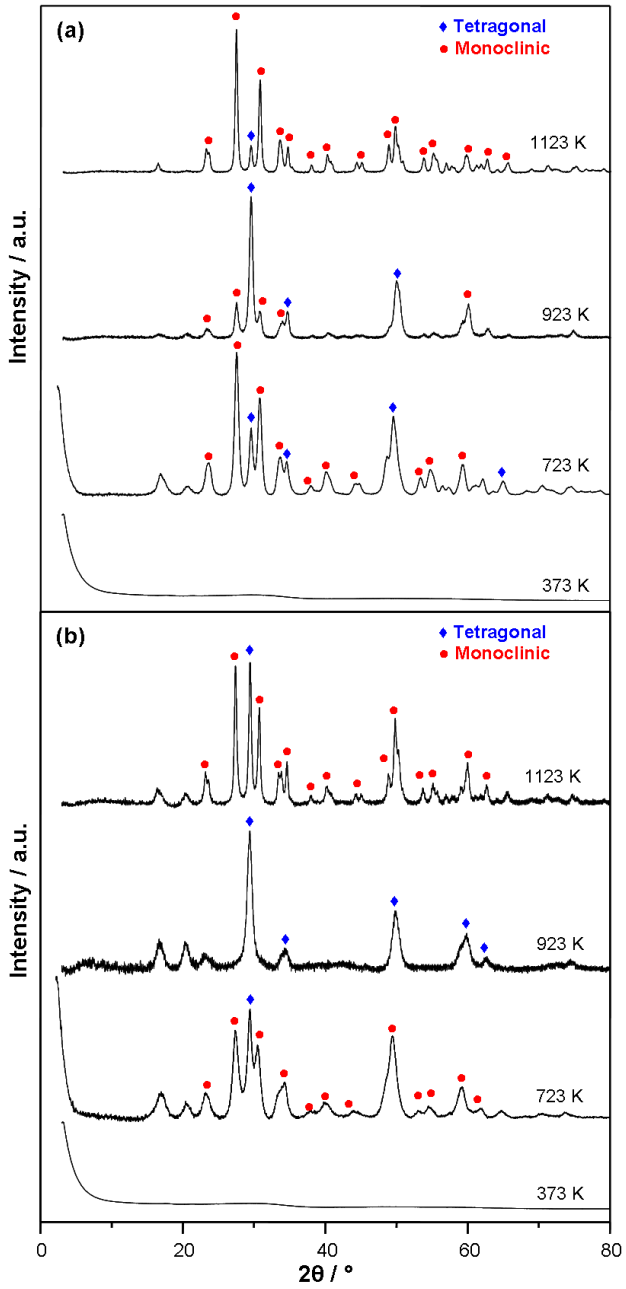

Fig. 3. 21 XRD diagrams of the zirconium/Brij56® obtained from (a) $ZrOCl_2.8H_2O$ and (b) $Zr(OC_2H_5)_4$ precursors after being annealed at different temperatures.

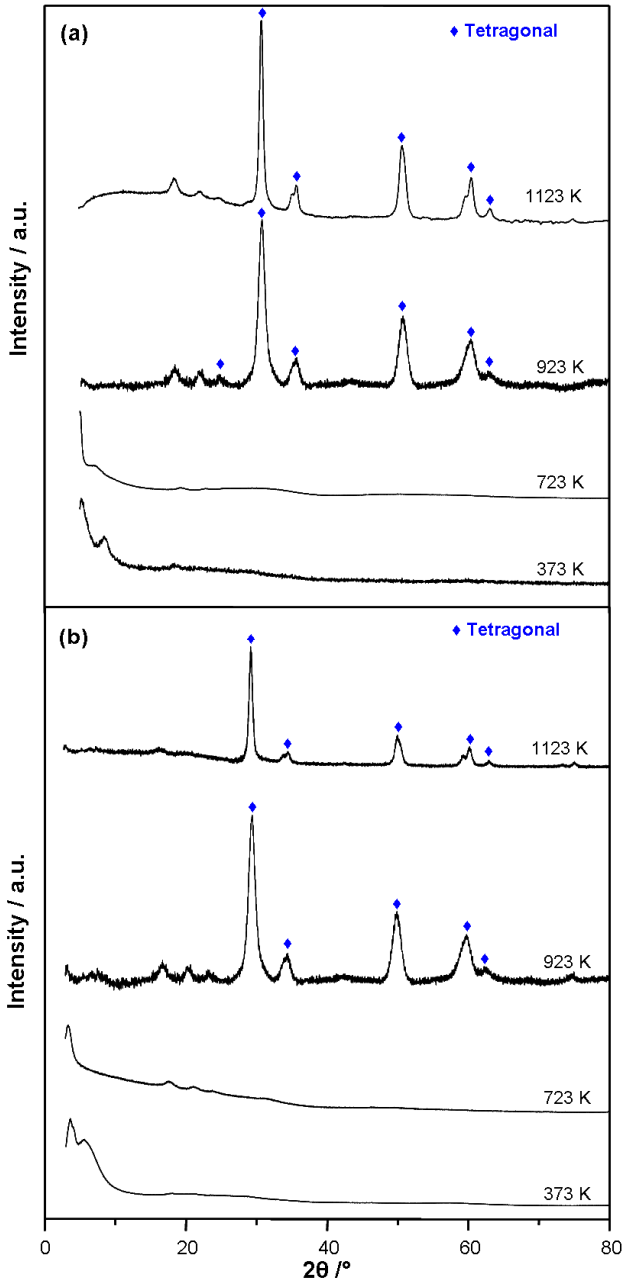

Fig. 3. 22 XRD diagrams of the zirconium/CTAB obtained from (a) $ZrOCl_2.8H_2O$ and (b) $Zr(OC_2H_5)_4$ precursors after being annealed at different temperatures.

3.2.2. Thermal Decomposition Analyses

TG and DTA analysis of as-prepared sample obtained from $ZrOCl_2.8H_2O$ precursor and its mass spectroscopy profile are shown in Fig. 3.23. Three molecular fragments were selected to detect by the mass detector: H_2O, O_2 and CO_2. The DTA curve presents two major exothermic peaks. The first exothermic peak observed at around 645 K is due to the decomposition of the surfactant CTAB and transformation of the sample into ZrO_2. This peak can be accompanied with the weight loss between 500 and 720 K. Fig. 3.23 also shows that between this temperature range, MS curve exhibits consumption of oxygen with evolution of H_2O and CO_2 occurring at around 650 K. This indicates the decomposition of the surfactant which was proved by the FTIR results of the samples annealed at 723 K showing no characteristic peak of CTAB. The second exothermic peak at 850 K is attributed to the crystallization of amorphous zirconia and removal of the surfactant residuals. As strong ionic bond was formed between surfactant head group and zirconium salt, it is more difficult to break these bond and higher temperatures were needed. Removal of the organic compound residue was also proven by the evolution of CO_2 and consumption of O_2 at around 830 K in Fig. 3.23.

The first weight loss in TG curve below 500 K, shown in Fig. 3.23, can be attributed to the removal of the physically absorbed water. Although, the endothermic peak corresponding to this process does not appear in the DTA curve, it was proved by the evolution of water in MS curve.

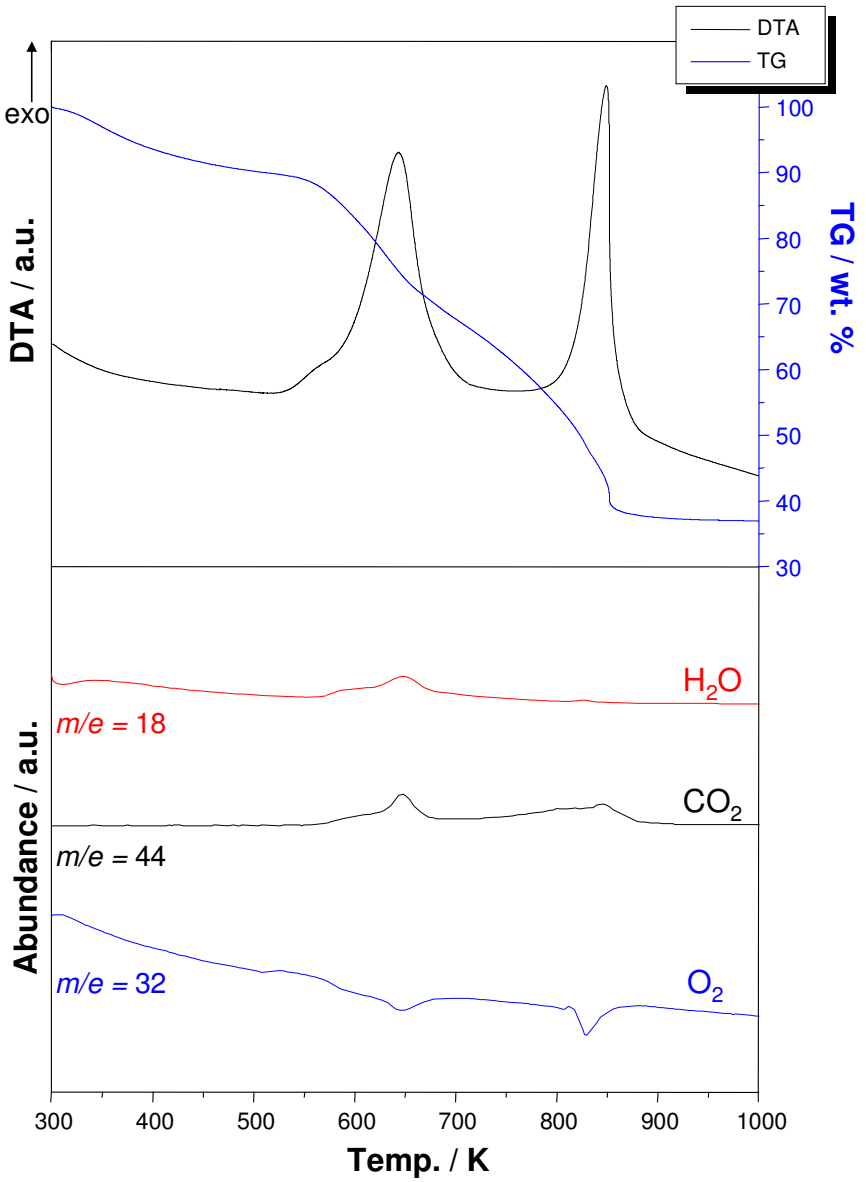

Fig. 3. 23 DTA-TG-MS curves for as-prepared sample obtained from $ZrOCl_2.8H_2O$ precursor under synthetic air

3.2.3. Fourier Transform Infrared Analysis

As-prepared and annealed samples were characterized by FTIR in order to investigate the interaction between CTAB templates and $ZrOCl_2.8H_2O$ precursors. In Fig. 3.24, spectra of as-prepared sample and pure CTAB are shown. Presence of two absorption bands at 2850 and 2918 cm^{-1} are corresponding to the symmetric and asymmetric C-H stretching vibrations of the hydrocarbon tail of CTAB, respectively. The tail group also causes the CH_2 scissoring vibration peaks at 1462 and 1486 cm^{-1}. In the spectrum of as-prepared sample shown in 3.24(a), the peaks in the region of 1400-900 cm^{-1} could be assigned to the vibrational band of the sulfate group. Strong bands around 3000-3600 cm^{-1} and 1636 cm^{-1} in this spectrum are due to the stretching and bending vibrations of absorbed water of as-prepared sample. The N-H stretching bands of the surfactant head group was not observed at around 3430 cm^{-1} in Fig. 3.24(b) due to the broad O-H stretching vibration in the as-prepared sample spectrum. Furthermore, the C-N stretching vibration of the head group of surfactant is at 1244 cm^{-1} while this absorption band undergoes red-shift to 1235 cm^{-1}. This red-shift indicates that the head group of surfactant coordinated to oxygen of the $ZrOCl_2.8H_2O$ precursor.

Moreover, after the as-prepared samples annealed at 723 K, all the vibrational bands relative to CTAB disappeared, evidencing the removal of the organic template by this process which is shown in Fig. 3.25(a). The band of Zr-O stretching vibration at 607 cm^{-1} becomes prominent emphasizing the formation of zirconium. In addition, there are O-H stretching and bending bands at around 2400-3670 cm^{-1} region and 1636 cm^{-1} due to the surface adsorbed water. The absorption bands in the 900-1400 cm^{-1} region which is assigned to the sulfate group shrinks with the heat-treatment.

The FTIR results give important clues about the self-assembly formation mechanism of CTAB and nanoporous zirconia formation. Fig. 3.26 is illustrates the schematic

representation of these processes. CTAB is a cationic surfactant with the CH_3-CH_3-CH_3-N structure. The repulsive interactions between hydrophobic tail, cationic head group and polar water medium, the surfactant self-organize into the sphere-rod transition of micelles in the presence of counter ion like SO_4^{2-}. The hydrophobic tail group tends to minimize the interaction with the water molecules, while the cationic head group tends to stay outside. When CTAB solution is introduced into $ZrOCl_2.8H_2O$ solution, cationic head groups interact with negatively charged zirconium salt through electrostatic interactions. This process leads to a formation of inorganic-surfactant composites in which CTAB serves as a template. After the formation of composite, hydrolysis and polymerization of zirconia takes place around the preformed rod-shaped micelles of surfactant, in the presence of sodium hydroxide.

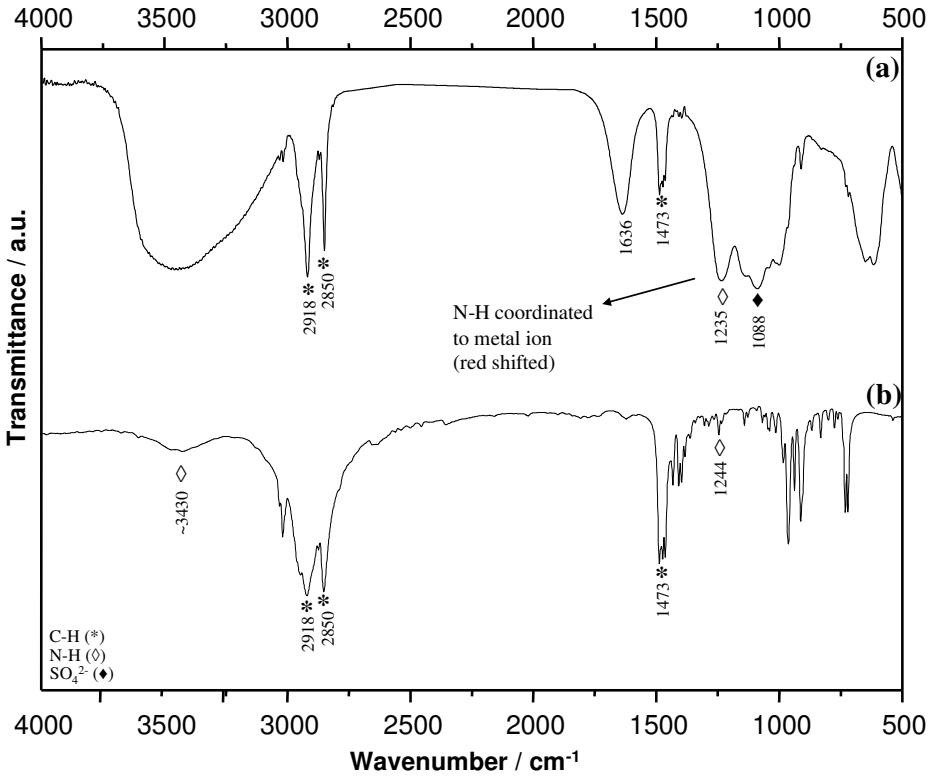

Fig. 3. 24 FTIR spectrum of (a) as-prepare sample and (b) pure CTAB

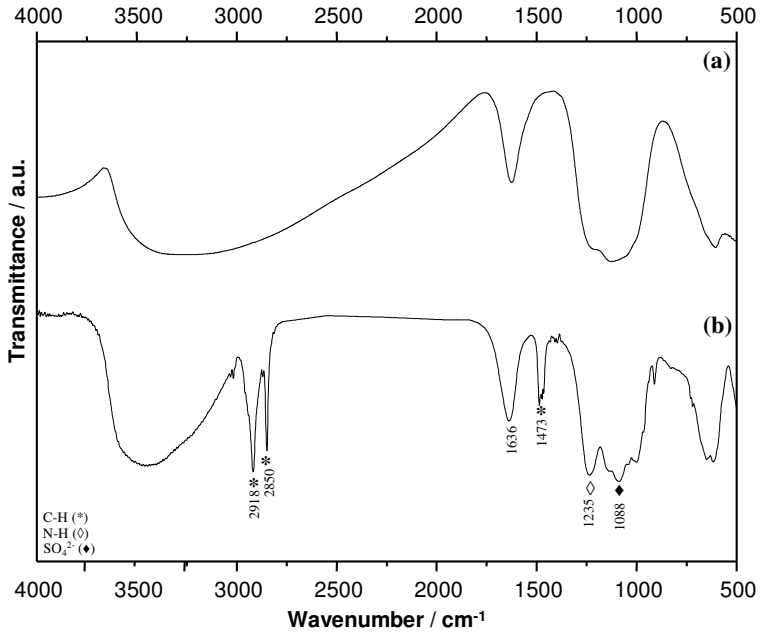

Fig. 3. 25 FTIR spectrum of (a) as-prepare sample and (b) annealed sample at 723 K

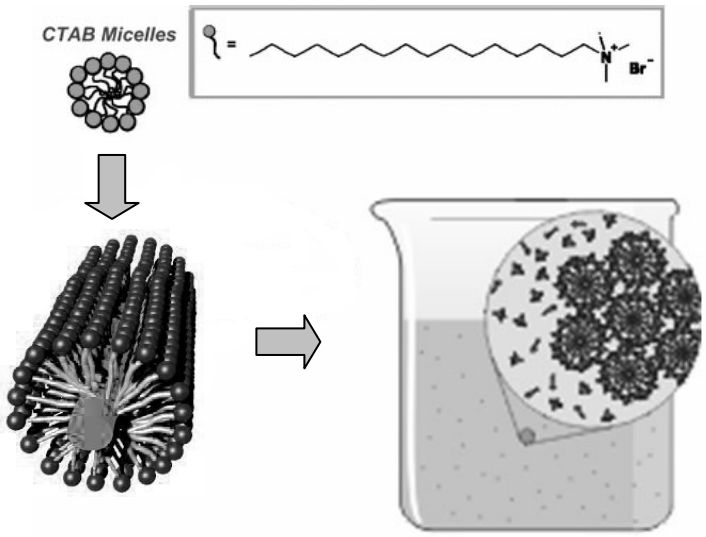

Fig. 3. 26 Schematic representation for the mechanism of the CTAB self-assembly and formation of porous zirconia

3.2.4. High Resolution Transmission Electron Microscopy Analysis

The HR-TEM images of annealed samples prepared via different methods are shown in Fig. 3.27. The samples treated with non-ionic surfactant Brij56® showed porous structure with random pore shapes and very high pore size distribution. On the other hand, only on some part of the sample, narrow pore size distribution and ordered identical pores can be observed in $Zr(OC_2H_5)_4$/CTAB composite.

Fig. 3.28 shows the HR-TEM image of zirconia prepared with $ZrOCl_2.8H_2O$ precursor and CTAB. The ordered pore arrangement was clearly visible. The pore size was calculated from the HR-TEM image and it was around 2.8 nm. As a result, it can be concluded that the sample is mesoporous zirconia.

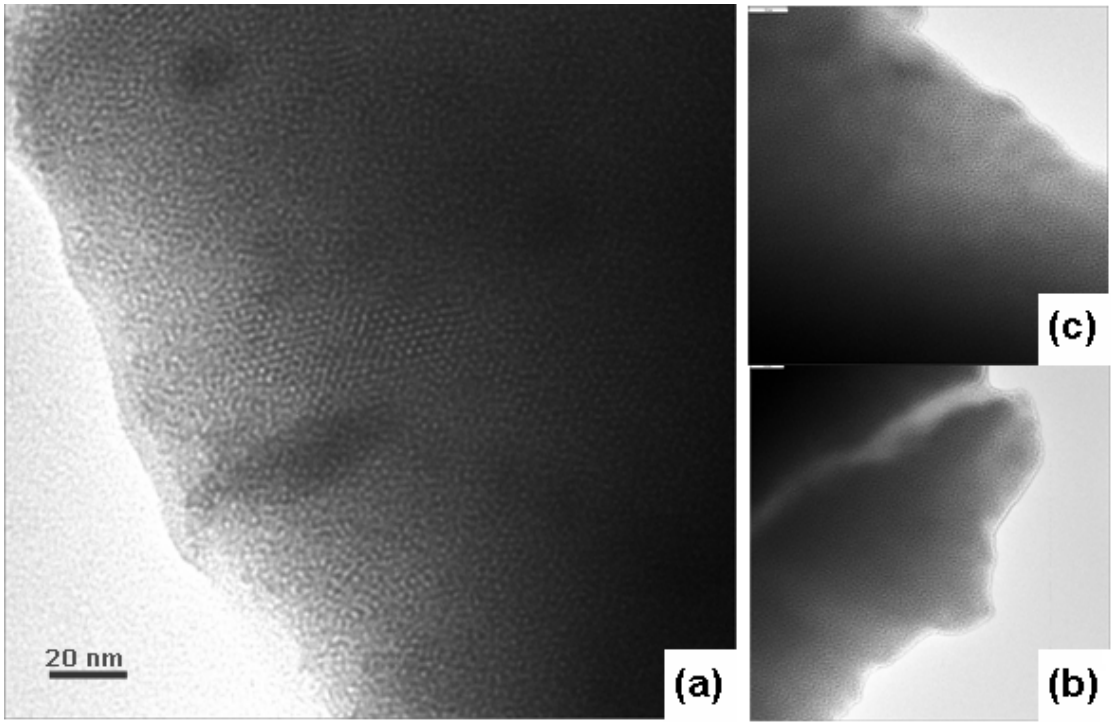

Fig. 3. 27 HR-TEM images of (b) $Zr(OC_2H_5)_4$/CTAB, (b) $ZrOCl_2.8H_2O$/Brij56® and (c) $Zr(OC_2H_5)_4$/Brij56® composites after being annealed at 723 K for 5 h.

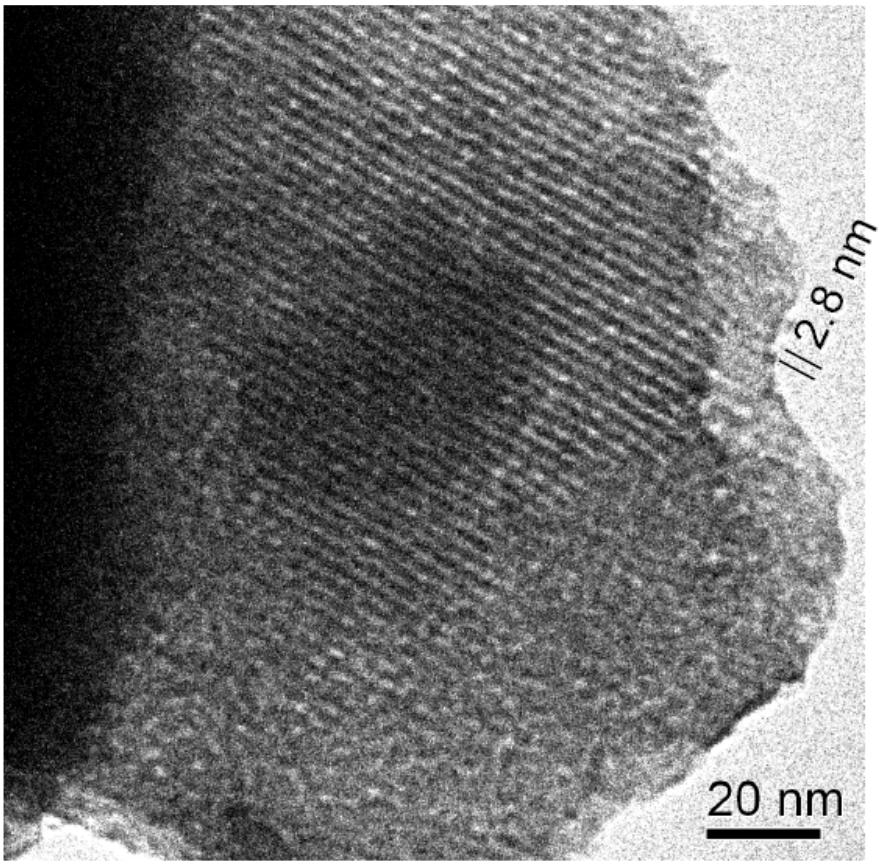

Fig. 3. 28 HR-TEM image of $ZrOCl_2.8H_2O$/CTAB composite after being annealed at 723 K for 5 h.

Chapter 4

CONCLUSION

The synthesis of rare earth oxides with controlled grain size was presented in the thesis work. In addition, two preparation route for the synthesis of nanostructured zirconium oxide was discussed in details.

In the first part, the investigations were focused on the preparation of nano-sized rare earth oxides via two synthesis routes, namely, liquid crystal templating and sol-gel method. The liquid crystal templating with oligo(ethylene oxide) type of non-ionic surfactant was applied to obtain nano-sized rare earth oxide particles with ~10 nm grain sizes. In these method, rare earth nitrates, $RE(NO_3)_3.nH_2O$ (n = 4-6; RE = Pr, Nd, Sm, Eu, Gd, Dy, Ho, Er, Tm, Yb, Lu) and non-ionic surfactant $C_{12}H_{25}(CH_2CH_2O)_{10}OH$ was used as rare earth source and surface-active agent, respectively. Among various salt/surfactant ratios, the ratio 1:6 was found to be optimal one because of the final particle size. Liquid crystal mesophases formation between rare earth nitrate and surfactant was achieved by dissolving the salt in the surfactant at 333 K. Here, the hydrogen bonding interaction between the coordinated water molecules of the salt and ethoxy head groups of the surfactant molecules induces the self-assembly of the surfactant molecules into complex nanoscale structures. Because of the repulsive forces between the head group and tail group, the head groups of the surfactant molecules tend to minimize the surface energy by forming reverse micelle structures with the salts. The head groups and the salt molecules are located in the core of the reverse micelles and this allows uniform distribution of the rare earth ions into these structures. The hydrogen bonding interaction which plays a key role in the formation of liquid crystal mesophase was proved with the FTIR results where the C-O stretching mode

of the pure surfactant molecules undergoes red-shift in the liquid crystal mesophases. Further, passing gaseous ammonia through this liquid crystal mesophase yields gelatinous hydroxide precipitates. The XRPD and HR-TEM results reveal that hydroxide and oxides were formed at the same time but they gave too weak or no reflections in the XRPD diffractions due to their very disordered structures. The pure rare earth oxides were obtained after heat-treatment at 773 K under air atmosphere. In contrast, neodymium sample absorbed CO_2 from the air and yielding oxide carbonate, $Nd_2O_2CO_3$, when annealed under air atmosphere. Though, it decomposed to pure Nd_2O_3 in the presence of synthetic air. According to HR-TEM results, both as-prepared and annealed samples revealed disordered structures. Indeed, the average particle sizes of the annealed samples are found to be ranging between 7 and 30 nm, which is in good agreement with the results calculated from the XRPD experiments with Debye-Scherrer's equation.

In the second method, sol-gel route was developed to prepare nanoparticles of Eu_2O_3, Gd_2O_3 and Er_2O_3 with average particle sizes of 34, 21 and 10 nm, respectively. The precursor $RE(NO_3)_3.nH_2O$ (n = 4-6; RE = Eu, Gd Er) was dissolved in mixture of diethylene glycol (DEG) and tetraethylene glycol (TEG). By passing gaseous ammonia through this suspension, reactive $RE(OH)_3$ precipitation was carried out. Hydrolysis of gaseous ammonia with the free water molecules of the system yielded rare earth hydroxides. The particle-particle aggregation is hindered by the high viscosity of polyalcohol mixture. The final pure rare earth oxides were obtained after annealing at 773 K. The prepared Eu_2O_3 powders were successfully dispersed in a mixture of water and acrylic acid. The dispersed oxides were then infiltrated into Al_2O_3 inverse opals by spin-coating. Optical microscopy images show that successful infiltration was carried out. The characteristic red luminescence of Eu_2O_3 was obtained when the infiltrated inverse opals were illuminated by 355 nm laser light.

In the second part of the study, two different routes based on surfactant templating were used for the preparation of nanoporous zirconia. The synthesis was carried out in the presence of two series of precursors, namely, $ZrOCl_2.8H_2O$ and $Zr(OC_2H_5)_4$.

In the first method, ordered mesoporous zirconia was obtained by using cationic surfactant hexadecyl-trimethyl-ammonium bromide, $CH_3(CH_2)_{15}N(CH_3)_3Br$, denoted as CTAB as the pore-directing agent. According to the HR-TEM results, zirconium oxide treated with $ZrOCl_2.8H_2O$ precursor possessed ordered pore structure at 723 K with narrow pore size distribution. The average pore size of this uniform pores are found to be 2.8 nm. The XRD results indicate that sample had amorphous pore walls at 723 K and formation of zirconia tetragonal phase was observed at 923 K. In the presence of counter ion SO_4^{2-} and water, the surfactant CTAB self-organized into the rod-shaped micelles. Because of the repulsive interaction between hydrophobic tail, cationic head group and polar water, the hydrocarbon group of CTAB molecules tends to minimize their interaction with water molecules, while the cationic head group tends to stay in the surface of the rod-shaped micelles. When these micelles introduced to precursor solution, the cationic head group of CTAB molecules interacts with negatively charged zirconium salt through electrostatic attraction. This attraction cause zirconium salts in the solution The FTIR results show that in the $ZrOCl_2.8H_2O$/CTAB composite, C-N stretching vibration of the head group of the CTAB molecule undergoes red-shift compared to that of the pure CTAB. This indicates that CTAB molecules interact with zirconium ions through negatively charged oxygen of the $ZrOCl_2.8H_2O$ precursor. In the zirconia sample prepared with precursor $Zr(OC_2H_5)_4$, nanoporous structure with non-uniform pores were observed. The HR-TEM results reveal that that sample possessed partial ordered pore structure with hexagonal arrangement and pore sizes were ranging from 0.1 to 1 nm. Both nanoporous zirconia prepared with $ZrOCl_2.8H_2O$ and $Zr(OC_2H_5)_4$ precursors showed similar thermal behavior with having amorphous structure below 923 K. Further heating leads to formation of the t-phase of

zirconia. In the second method, which is liquid crystal templating with non-ionic surfactant $C_{12}H_{25}(CH_2CH_2O)_{10}OH$, porous zirconia was prepared. In these method, $ZrOCl_2.8H_2O$ and $Zr(OC_2H_5)_4$ were used as a zirconium source and non-ionic surfactant Brij56® was a pore-templating agent. Liquid crystal mesophase of zirconium precursor and surfactant was achieved by dissolving the salt in melted surfactant. According to the HR-TEM images, non-ionic surfactant leads smaller pores with high pore size distribution.

VITA

Atilla Aşar was born in Balıkesir, Turkey, on June 19, 1984. He completed high school in Balıkesir Sırrı Yırcalı Anadolu Lisesi in 2002. He received his degree of Bachelor of Science in Chemistry Koç University, Istanbul, in 2007. The same year, he started his Master studies in the program Material Science and Engineering at Koç University.

BIBLIOGRAPHY

[1] Henglein, A., *Small-particle research: Physicochemical properties of extremely small colloidal metal and semiconductor particles.* Chemical Reviews, 1989. **89**(8): p. 1861–1873.

[2] Alivisatos, A.P., *Perspectives on the physical chemistry of semiconductor nanocrystals.* Journal of Physical Chemistry, 1996. **100**(31): p. 13226-13239.

[3] Roduner, E., *Nanoscopic materials: Size-dependent phenomena*. 2006, Cambridge: The Royal Society of Chemistry.

[4] Klabunde, K.J., *Nanoscale materials in chemistry*. 2001, New York: A John Wiley & Sons, Inc.

[5] Roduner, E., *Size matters: Why nanomaterials are different.* Chemical Society Reviews, 2006. **35**: p. 583-592.

[6] Sun, S. and C. Murray, *Synthesis of monodisperse cobalt nanocrystals and their assembly into magnetic superlattices.* Journal of Applied Physics, 1999. **85**: p. 4325–4330.

[7] Eychmüller, A., *Structure and photophysics of semiconductor nanocrystals.* Journal of Physical Chemistry B, 2000. **104**(28): p. 6514–6528.

[8] Kruis, F.E., H. Fissan, and A. Peled, *Synthesis of nanoparticles in the gas phase for electronic, optical and magnetic applications.* Journal of Aerosol Science, 1998. **29**(5-6): p. 511-535

[9] *TU Delft. Faculty of Applied Sciences*. [cited; Available from: http://www.tnw.tudelft.nl/live/pagina.jsp?id=5550e07d-ec54-4f77-bcf0-5736863ef4b8&lang=en.

[10] Oyewumi, M. and R. Mumper, *Gadolinium-loaded nanoparticles engineered from microemulsion templates.* Drug Development and Industrial Pharmacy, 2002. **28**(3): p. 317-328

[11] Gerberich, W.W., et al., *Superhard silicon nanospheres.* Journal of the Mechanics and Physics of Solids, 2003. **51**(6): p. 979-992.

[12] Wakefield, G., et al., *Synthesis and properties of sub-50-nm europium oxide nanoparticles.* Journal of Colloid and Interface Science, 1999. **215**(1): p. 179-182.

[13] Yamamoto, Y., et al., *Magnetic properties of the noble metal nanoparticles protected by polymer.* Physica B: Condensed Matter (Amsterdam), 2003. **329–333**(2): p. 1183-1184.

[14] Greenwood, N.N. and A. Earnshaw, *Chemistry of the Elements*. 1997, Oxford: Butterworth-Heinemann.

[15] Goubard, F., et al., *Synthesis and luminescent properties of PEO/lanthanide oxide nanoparticle hybrid films.* Journal of Luminescence, 2007. **126**(2): p. 289-296.

[16] Adachi, G., N. Imanaka, and Z.C. Kang, *Binary rare earth oxides*, ed. G. Adachi. 2004, Amsterdam: Kluwer Academic Publishers.

[17] Grangvist, C.G., L.B. Kish, and W.H. Marlow, *Gas phase nanoparticles synthesis*. 2004, New York: Springer.

[18] Xu, C., et al., *Submicron-sized spherical yttrium oxide based phosphors prepared by supercritical CO_2-assisted aerosolization and pyrolysis.* Applied Physics Letter, 1997. **71**: p. 1643-1649

[19] Kang, Y.C., et al., *Gd_2O_3:Eu phosphor particles with sphericity, submicron size and non-aggregation characteristics.* Journal of Physics and Chemistry of Solids 1999. **60**(3): p. 379-384.

[20] Uekawa, N., et al., *Synthesis of CeO_2 spherical fine particles by homogeneous precipitation method with polyethylene glycol.* Chemistry Letters 2002. **31**(8): p. 854-855

[21] Li, M., et al., *The study on the preparation methods and the fluidity of large rare earth oxide particles.* Colloids and Surfaces A: Physicochemical and Engineering Aspects, 2008. **320**(1-3): p. 78-84.

[22] Tok, A.I.Y., et al., *Hydrothermal synthesis and characterization of rare earth doped ceria nanoparticles.* Materials Science and Engineering: A, 2007. **466**(1-2): p. 223-229

[23] Huang, G., et al., *Synthesis of yttrium oxide nanocrystal via solvothermal process.* Journal of Rare Earths, 2006. **24**(1): p. 47-50.

[24] Fang, Y.-P., et al., *Hydrothermal synthesis of rare earth (Tb, Y) hydroxide and oxide nanotubes.* Advanced Functional Materials, 2003. **13**(12): p. 955 - 960.

[25] Guo, B., et al., *Atmospheric pressure synthesis of heavy rare earth sesquioxides nanoparticles of the uncommon monoclinic phase.* Journal of the American Ceramic Society, 2007. **90**(11): p. 3638-3686.

[26] Hu, L., et al., *Oriented monolayer film of Gd_2O_3:0.05 Eu crystallites: Quasi-topotactic transformation of the hydroxide film and drastic enhancement of photoluminescence properties.* Angewandte Chemie, 2009. **121**(21): p. 3904-3907

[27] Kang, Y.C., et al., *Preparation of nonaggregated Y_2O_3 :Eu phosphor particles by spray pyrolysis method.* Journal of Materials Research, 1999. **14**(6): p. 2611-2615.

[28] Hannink, H.J., *Nanostructure control of materials*. 2006, Cambridge: Woodhead.

[29] Zhu, B., et al., *Solid oxide fuel cell (SOFC) using industrial grade mixed rare-earth oxide electrolytes.* International Journal of Hydrogen Energy, 2008. **33**(13): p. 3385-3392

[30] Guanming, Q., et al., *Application of rare earths in advanced ceramic materials*

Journal of Rare Earths, 2007. **25**(2): p. 281-286

[31] Yada, M., et al., *Rare earth (Er, Tm, Yb, Lu) oxide nanotubes templated by dodecylsulfate assemblies.* Advanced Materials, 2002. **14**(4): p. 309-3013.

[32] Sing, K.S.W., et al., *Reporting data for physisorption data for gas/solid systems with special reference to the determination surface area and porosity.* Pure and Applied Chemistry, 1985. **57**(4): p. 603-619.

[33] Ishizaki, K., S. Komarneni, and M. Nanko, *Porous materials: Process technology and applications*, ed. K. Ishizaki. 1998, Boston: Kluwer Academic Publishers.

[34] Polarz, S. and B. Smarsly, *Nanoporous materials.* Journal of Nanoscience and Nanotechnology, 2002. **2**(6): p. 581-612.

[35] Kresge, C.T., et al., *Ordered mesoporous molecular sieves synthesized by a liquid-crystal template mechanism.* Nature, 1992. **359**: p. 710-712.

[36] Lu, G.Q., *Nanoporous materials: Science and Engineering*. 2004, London: Imperial College Press.

[37] Trivinho-Strixinoa, F., F.E.G. Guimarães, and E.C. Pereira, *Zirconium oxide anodic films: Optical and structural properties.* Chemical Physics Letters, 2008. **461**(1-3): p. 82-86

[38] Tanabe, K. and T. Yamaguchi, *Acid-base bifunctional catalysis by ZrO_2 and its mixed oxides.* Catalysis Today, 1994. **20**(2): p. 185-197.

[39] Rosa, E.D.l., et al., *Visible light emission under uv and ir excitation of rare earth doped ZrO_2 nanophosphor.* Optical Materials, 2005. **27**(7): p. 1320-1325

[40] Pulickel M. Ajayan, Linda S. Schadler, and P.V. Braun, *Nanocomposite Science and Technology* 2003: John Wiley and Sons, Inc.

[41] Samarskaya, O. and O. Dag, *Silver nitrate-oligo(ethylne oxide) surfactant-mesoporous silica nanocomposite films and monoliths.* Journal of Colloid and Interface Science, 2001. **238**(1): p. 203-207.

[42] Dag, O., et al., *Salted mesostructures: Salt-liquid crystal templating of lithium triflate-oligo(ethylene oxide) surfactant-mesoporous silica nanocomposite films and monoliths.* Journal of Materials Chemistry, 1999. **9**: p. 1475 - 1482.

[43] Dag, O., et al., *Oriented periodic mesoporous organosilica (PMO) film with organic functionality inside the channel walls.* Advanced Functional Materials, 2001. **11**(2): p. 213-217.

[44] Attard, G., J. Glyde, and C. Göltner, *Liquid-crystalline phases as templates for the synthesis of mesoporous silica.* Nature, 1995 **378**: p. 366 - 368.

[45] Dag, O., S. Alayoglu, and I. Uysal, *Effects of ions on the liquid crystalline mesophase of transition-metal salt:Surfactant (C_nEO_m).* Journal of Physical Chemistry B, 2004. **108**(24): p. 8439–8446.

[46] Tura, C., N. Coombs, and O. Dag, *One-pot synthesis of cds nanoparticles in the channels of mesostructured silica films and monoliths.* Chemistry of Materials, 2005. **17** (3): p. 573–579.

[47] Celik, Ö. and Ö. Dag, *A new lyotropic liquid crystalline system: Oligo(ethylene oxide) surfactants with $[M(H_2O)_n]_{xm}$ transition metal complexes* Angewandte Chemie International Edition, 2001. **113**(20): p. 3915 - 3919.

[48] Mazdiyasni, K.S. and L.M. Brown, *Microstructure and electrical properties of sc_2o_3-doped, rare-earth-oxide-doped, and undoped $BaTiO_3$.* Journal of the American Ceramic Society, 1971. **54**(11): p. 539-543

[49] Feldmann, C. and H.-O. Jungk, *Polyol mediated preperation of nanosclae oxide particles.* Angewandte Chemie International Edition, 2001. **113**(2): p. 372 – 374.

[50] Knowles, J.A. and M.J. Hudson, *Preparation and characterization of mesoporous, high surface area zirconium(IVv) oxides.* Journal of Chemical Society, 1995. **20**: p. 2083 - 2084.

[51] Sanchez, C., et al., *Nanocrystalline transition-metal oxide spheres with controlled multi-scale porosity.* Advanced Functional Materials, 2003. **13**(1): p. 37-42.

[52] Su, C., et al., *Synthesis of isobutene from synthesis gas over nanosize zirconia catalysts.* Applied Catalysis A: General, 2000. **202**(1): p. 81-89

[53] Suh, D.J., et al., *Synthesis of high-surface-area zirconia aerogels with a well-developed mesoporous texture using CO_2 supercritical drying.* Chemistry of Materials, 2002. **14**(4): p. 1452–1454.

[54] Ciesla, U., et al., *Formation of a porous zirconium oxo phosphate with a high surface area by a surfactant-assisted synthesis.* Angewandte Chemie International Edition, 1996. **35**(5): p. 541-543

[55] Crepaldi, E., et al., *Control formation of highly ordered cubic and hexagonal mesoporous nanocrystalline yttria-zirconia and ceria-zirconia thin films exhibiting high thermal stability.* Angewandte Chemie International Edition, 2003 **42**(3): p. 347-351.

[56] *Stoe WinxPow 1.2*. 2000, Stoe & Cie GmbH: Darmstadt.

[57] *Inorganic Crystal Structure Database (icsd)*. 2009, FIZ Karlsruhe.

[58] Jasco, *Model FT/IR -600 plus function manual* 2001.

[59] Boulch, F., et al., *Domain size distribution of Y-TZP nano-particles using XRD and HR-TEM* Image Analysis & Stereology, 2001. **20**(3): p. 157-161.

[60] Cao, G., *Nanostructures and nanomaterials: Synthesis, properties and applications*. 2004, London: Imperial College Press Inc.

[61] Minero, C., et al., *One-electron transfer equilibriums and kinetics of n-methylphenothiazine in micellar systems.* Journal of Physical Chemistry, 1983. **87**(3): p. 399–407.

[62] Rosen, M.J., *Surfactants and Interfacial Phenomena*. 1978, New York: John Wiley & Sons.

[63] Lopez, C., *Materials aspects of photonic crystals.* Advanced Materials, 2003. **15**(20): p. 1679-1704.

[64] Lopez, C., *Three-dimensional photonic bandgap materials: Semiconductors for light.* journal of Optics A: Pure and Applied Optics 2006. **8**: p. R1-R14.

[65] Lopez, C., *Photonic bandgap engineering in germanium inverse opals by chemical vapor depostion.* Advanced Materials, 2001. **21**(13): p. 1634-1638.

[66] Luo, T.Y., T.X. Liang, and C.S. Li, *Stabilization of cubic zirconia by carbon nanotubes.* Materials Science & Engineering, A: Structural Materials: Properties, Microstructure and Processing, 2004. **366**(a): p. 206-209.